Diamond & Related Materials 164 (2026) 113511

Contents lists available at ScienceDirect

Diamond & Related Materials

journal homepage: www.elsevier.com/locate/diamond

Nanomechanical properties, residual stress, and microstructure of graphene-like/diamond (sp^2/sp^3 C) covalent heterostructures

Sanju Gupta [b,a,*], Katarzyna Bury [c], Paul W. May [d]

[a] Department of Physics and Astronomy, University of Georgia, Athens, GA, 30602, USA
[b] Department of Optoelectronics, Faculty of Electronics, Telecommunication and Informatics, Gdańsk University of Technology, Narutowicza Str. 11/12, 80-233, Gdańsk, Poland
[c] Laboratory of Molecular Biology, Intercollegiate Faculty of Biotechnology UG/MUG, Abrahama 58, 80-307, Gdańsk, Poland
[d] School of Chemistry, University of Bristol, Bristol, BS8 1TS, UK

ARTICLE INFO

Keywords:
MPACVD
BCNW/diamond heterostructures
rGO/diamond
Microstructure
Non-destructive evaluation
Nanomechanical properties

ABSTRACT

Carbons with different chemical bonding, diamond (sp^3) and graphene (sp^2), are the building blocks for a new class of all-carbon structures, where different allotropic carbon networks interact, coexist, reconstruct, and transform. We report integration of diamond with graphene-like structures, offering a versatile playground for electronic devices and nano-/micro-electromechanical (N/MEMS) systems. To utilize these covalent heterostructures, understanding and linking their microstructure and physical properties becomes indispensable. Polycrystalline diamond films were grown on seeded Si(001) substrates using microwave plasma-assisted and hot-filament chemical vapor deposition with methane in high hydrogen dilution and B_2H_6 for boron doping, followed by selective area deposition of B-doped carbon nanowalls (BCNW) and subsequent diamond layer, allowed to form various interfaces (BCNW/Diam. and Diam./BCNW/Diam.), besides drop-cast reduced graphene oxide (rGO) layer on undoped diamond ($rGO/Diam._{HFCVD}$). We determined residual stress using XRD and micro-Raman spectroscopy and measured force-deflection curves, i.e., force felt by AFM tip as it approached and retracted from the sample surface. Force volume spectroscopy acquires an array of curves over an extended area, gaining insights into interfacial bonding and distribution of nanoscale intermolecular forces (Young's modulus, stiffness, adhesion). The structures demonstrate that BCNW intertwined with diamond (111) crystallites and B-doping significantly influence elastic moduli distribution. Meanwhile, information in FV decoupled from topographic data, and the Young's moduli and mechanical strength estimated using principal contact mechanics models followed the order: $rGO/Diam._{HFCVD} \geq$ Diam./BCNW/Diam. $>$ BCNW/BDD $\geq$ Diam./*p*-Si(001). The findings are discussed in terms of surface, microstructure properties and restructuring of interfacial carbon atoms, providing stability of the resulting covalent configurations.

1. Introduction

Three-dimensional graphite and diamond were the only known natural allotropes of crystalline carbon [1,2] until the discovery of synthetic 0-dimensional fullerenes [3] and 1-dimensional carbon nanotubes [4], followed by the inception of 2-dimensional atomically thin carbon i.e., monolayer graphene [5]. A rejuvenated interest in diamond, a wide bandgap (~5.45 eV) semiconductor, has occurred for more than two decades due to its unique combination of extraordinary physical-chemical properties [6,7]. While natural diamond formation requires extreme pressures and temperatures [8], diamond thin films (DTF) grown using hot-filament (HFCVD) and microwave plasma-assisted chemical vapor deposition (MPACVD) techniques became useful for optical windows (wide spectral transparency), power electronics (high temperature and large breakdown voltage ~10^7 V/cm), biosensors (chemical inertness), tribological coatings to prevent wear and attrition and cutting tools yielding significant hardness to address extreme abrasion, heat sinks (high thermal conductivity), and have potential for emerging quantum information science and sensing with NV centers as well as neuromorphic engineering and therefore are central to the modern technological landscape [9,10,11,12]. Likewise, graphene and its variants, including graphene oxide, GO, its reduced form, rGO, and recently synthesized vertical carbon and graphene nanowalls [12,13,14,15,16], are equally promising, ensuring immense potential

* Corresponding author at: Department of Physics and Astronomy, University of Georgia, Athens, GA 30602 and Department of Optoelectronics, Faculty of Electronics, Telecommunication and Informatics, Gdańsk University of Technology, Narutowicza Str. 11/12, 80-233, Gdańsk, Poland.

https://doi.org/10.1016/j.diamond.2026.113511
Received 10 January 2026; Received in revised form 22 February 2026; Accepted 2 March 2026
Available online 5 March 2026

and versatility for emerging areas of clean energy, sensing, nanoscale electronics and photonics applications [17,18,19,20,21]. Therefore, in search for new structural topologies composed of elemental carbons of differing chemical bonding character is driven by technological opportunities as well as the need to understand the evolution and fate of carbon phases in laboratory syntheses.

The integration of carbons with different chemical bonding character, diamond (sp^3 tetrahedral coordination) and graphene (sp^2 trigonal planar coordination), that are at the opposite limits of carbon at the nanoscale, are the building block for a new class of functional all carbon systems [22,23,24,25,26]. The new family of diamond-graphene known as gradia when graphene monolayer is placed on diamond (van der Waals interaction) [27] and diaphite phase constructed from layered and bonded sp^3 and sp^2 nanostructured units at the interface following in-situ transformation leading to modulated covalent bonding that provide a framework for classifying members of this new class of hybrid carbon materials [28,29]. The diaphite-like nanocomposites represent high-performance materials that are predicted to combine the superhard qualities of diamond with high fracture toughness and ductility/conformability and conduction enabled by the graphitic units and the reconfigured diamond surface yet with defined interfaces between the sp^3- and sp^2-bonded nanodomains. Within this rein, the combination of diamond and graphene-like carbon nanowalls (CNW) [30,31] is generating an increasing attention, where differing carbon networks coexist, interact, reconstruct, and transform one into one another enabled by covalent interaction [32,33,34,35]. This interest invoked novel synthetic formulations that has gradually expanded, enabled by innovative in-situ methods providing novel strategies and benefits [36,37,38,39,40]. Because research efforts so far have concentrated primarily on synthesis optimization to produce highly crystalline and textured, undoped and boron-doped diamond (BDD) and B-doped carbon nanowalls (BCNW) films for electrochemical and biochemical sensing applications. Their characteristics of rapid electron transfer and ion transportation were key for dynamic physicochemical processes, attributed to their large specific surface area, electrical conductivity, mechanically robust framework, thermal and chemical stability [36,41]. Attempts to obtain relatively smoother surfaces and interfaces usually result in a mixed yet balanced sp^3 and sp^2-bonded carbon, which are attractive for x-ray lithography masks, coating tools with extreme hardness and sliding parts [42,43], as cold cathodes for efficient field emission [44,45], SAW devices, micro-fluidics, memristors for alternative computing, nanomechanical resonators and other nano-/micro-electromechanical systems (N/MEMS) [12,46,47,48]. The promise of emerging diamond-graphene-like structures can be achieved through creating interfaces that enhance their chemical and mechanical properties by engineering the relative ratio and spatial correlation or surface hybridization of sp^3/sp^2 coordinated carbon atoms [49], which is the focus of current study. Alternatively, graphene-like layers placed on diamond films forming covalent heterostructures provides a new route to improve carrier transport and physical hardness characteristics of diamond unlike those offered from similar structures on SiO_2/Si substrates [50,51].

In this work, we synthesized polycrystalline diamond films with preferential ⟨111⟩ texture grown by MPACVD with low and high boron doping, followed by selective area deposition of BCNW forming BCNW/BDD covalent heterostructures and subsequent deposition of diamond film over BCNW/BDD forming a sandwich configuration such as Diam./BCNW/Diam. structure. As for the rGO/diamond covalent structure, the rGO was drop-casted selectively onto HFCVD deposited unintentional doped diamond film. We investigated their structural, physical, and nanomechanical properties using complementary analytical techniques to establish *microstructure-process-property* correlations from various technological standpoints, while discerning subtle variation in process parameters and how they affect nanomechanical properties. Moreover, this work reports interesting findings which relate and highlight similarities or disparities in a range of similar materials from those existing in the literature. Finally, we attempted to describe our findings of these all-carbon heterostructures in terms of interfacial registry via surface hybridization, bonding and restructuring model that provides fragile stability of the coordinated carbon atoms and fate of interphases at the nanoscale.

2. Experimental methods

2.1. Materials synthesis

Diamond thin films and carbon nanowalls with boron doping were synthesized using microwave plasma-assisted chemical vapor deposition (MPACVD) technique in a commercial CVD reactor (2.45 GHz SEKI Technotron AX5400S, Tokyo, Japan) on *p*-type Si (001) substrates (SIEGERT WAFER GmbH, Aachen, Germany) with and without SiO_2 and of float zone (Fz) type of 10 mm × 10 mm × 0.25 mm dimensions. All the substrates with some variations were seeded for ~30 min in an ultrasonication bath with laboratory prepared nanodiamond colloidal suspension consisting of 4–7 nm nanodiamond particles (NanoAmando Aqueous Colloid, NanoCarbon Research Institute, Ltd. Japan), washed with isopropyl alcohol (IPA) to remove excess seeding and dried with N_2 gas. The density of seeding in the range up to 10^{10} cm^{-2} was limited to minimize contribution of undoped seeds to the interfacial resistance as reported by Hantschel et al. [52]. The substrates were placed in the reaction chamber with a base pressure of 10^{-4} Torr. The temperature of the heated graphite stage was kept at 700 °C for diamond film and 850 °C for B-doped carbon nanowalls; BCNW. The temperature of the sample stage in the chamber was obtained using an induction heater. Diborane (B_2H_6) gas was used as the dopant precursor. The boron doping level in gas phase during deposition expressed as [B]/[C] ratio was kept at 1500–2000 ppm (BDD_l) and 4000–5000 ppm (BDD_h) for low and high doping, respectively and at 2000 ppm for BCNW layers. The plasma microwave power of 1300 W was applied for all deposition steps. The growth time was set between 6 and 7 h for diamond and 25–30 min for BCNW. The entire fabrication process consisted of two steps resulting in the allotropic carbon heterostructures junctions studied in this work. In the first step, the polycrystalline diamond layer with carrier density of 10^{17}–10^{18} cm^{-3} was deposited followed by selective deposition of BCNW via masking diamond films deposited in the previous step with a piece of silicon place. Growth occurred on the exposed area of the diamond film as the second step, forming BCNW/Diam. (CD1), followed by diamond film grown on CD1, resulting in Diam./BCNW/Diam. (DCD1) heterostructures. For diamond film without boron deposited using hot-filament CVD (HFCVD), Si(001) substrates were seeded in similar manner as for MPACVD, followed by growth with 1%CH_4 in high hydrogen dilution (99%H_2) at 700 °C deposition temperature for four hours resulting in thickness of ~2 μm. We drop-cast reduced graphene oxide; rGO, prepared by low temperature thermal reduction of graphene oxide (GO) at 180 °C leading to C:O = 10:1 on HFCVD deposited diamond film selectively forming rGO/Diam. (GD1) heterostructure and dried at 80 °C in air before physical property measurements. Fig. 1 provides a schematic diagram of various representative covalent heterostructures synthesized using MPACVD and HFCVD and detailed summary of the deposition parameters for samples under study are in Table 1 along with their nomenclature. All these materials are labeled from right to left according to the order in which they were grown.

2.2. Sample characterization

2.2.1. Surface morphology, microstructure, and physical properties

The samples were characterized to reveal surface morphology and microstructure. Scanning electron microscopy (SEM) images were taken with instrument (Model Prisma E Thermo Fisher Scientific, USA) operating at a primary electron acceleration voltage 15 kV and constant current 45 μA in secondary electron imaging (SEI) mode with a tungsten filament and at 45° angle for cross-sectional images. To obtain two- and

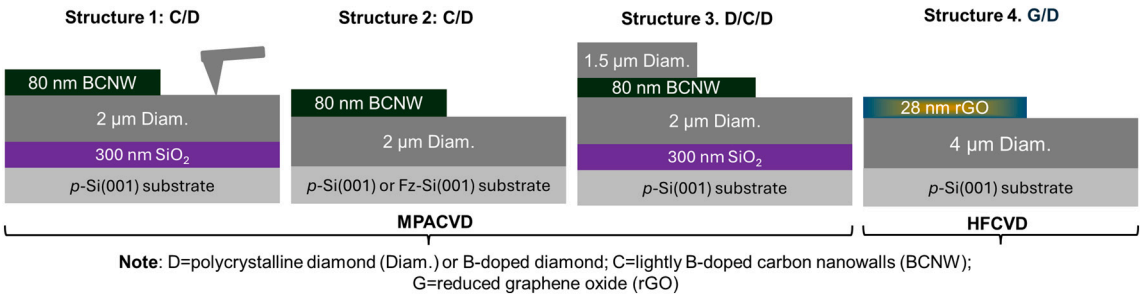

Fig. 1. Various carbon-based covalent heterostructures comprising graphene-like (sp^2 C) BCNW and rGO on polycrystalline diamond (sp^3 C) layers grown on seeded *p*-Si(001), SiO_2/*p*-Si(001) and *Fz*-Si(001) substrates.

three-dimensional topography, atomic force microscopy (AFM) Model BioScope Resolve AFM (Bruker, Bremen, Germany) operating in non-contact tapping mode was used to determine the average size distribution of crystallites and surface roughness quantitatively. A ScanAsyst-Air probe (Bruker Corp., Santa Barbara, CA) was used for imaging. Topographic images were registered at 512 × 512 pixels with silicon tip on nitride lever (Brukerafm probes) of spring constant $k = 0.8 \pm 0.05$ N/m, with Tapping frequency $f_0 = 70$ kHz (resonant frequency) and amplitude 145–150 nm. The scan speed varied depending on the image size that ranged from 0.6 to 5 μm/s, lateral optical level sensitivity of ≤1 μV and manufacturer's stated tip radius of curvature when first used was <30 nm. Before imaging, the cantilever spring constant was calibrated using the thermal tune method fundamental to quantitative force measurements. It is based on the equipartition theorem, which relates the cantilever's mean-square deflection to its spring constant and temperature [53]. As for determining the deflection sensitivity, it was carried out on a flat clean glass surface that converts the photodetector signal (usually in volts) to actual cantilevers defection (in nanometers), refers as inverse optical lever sensitivity and expressed as nm/V, following F [N] = k [N/m], InvOLS [m/V], and Deflection [V] [54]. The tip area was determined using direct imaging with electron microscopy.

For nanoscale morphology, a few flakes were distributed onto commercial carbon coated 300 mesh Cu grids (Ted-Pella, CA, USA) and analyzed with transmission electron microscope (TEM Model Tecnai Spirit BioTWIN) operating at 120 kV and 1 nA from LaB_6 gun with a Be specimen holder and with AMT 8 Mpixel cooled camera. For higher resolution TEM (Model Talos f200s 200 KV and FEI Noval 450 for FIB) was used to analyze nanoscale morphology for BCNW/Diam. interface. The bulk structure of thin films was analyzed with an X-ray diffractometer (Model Philips X'pert PRO with Anton Parr HTK-1000 camera) operating with CuK_α radiation ($\lambda = 1.54$ Å) in the range of $2\theta = 5°$–$95°$. Lattice vibrational spectra were recorded using a micro-Raman spectrometer equipped with a LEICA setup (Model InVia Renishaw *plc*, Hoffman Estates, IL, USA), Ar^+ laser of excitation wavelength $\lambda_L = 514$ nm ($E_L = 2.41$ eV) and 1800 lines/mm grating yielding spectral resolution of 1 cm^{-1}. The reflected light was filtered using an edge filter to remove laser excitation cutting at ~100 cm^{-1}. The scattered light from the sample was collected in backscattering geometry with an objective lens of ×50 providing a spot size ~1–2 μm defining the probe area. The laser power on the sample was maintained at 450 μW (0.45 mW) to prevent photothermal degradation. The Raman spectra were acquired for 100–120 s dwell time to maximize throughput signal. Raman spectra ranged between 100 and 3400 cm^{-1} depending upon whether the diamond (1000–2000 cm^{-1}) or BCNW or rGO (1000–3400 cm^{-1}) regions were acquired. Each sample was analyzed at randomly selected points and the spectra were averaged from those a few measurements. The intensity ratio was estimated by fitting Raman spectra with a Lorentzian profile.

To allow more detail and a greater understanding of the interaction between BCNW and rGO overlayers and diamond films underneath, we measured electrical (*I-V*) properties in the in-plane configuration. The room temperature resistivity was measured on the surface of all samples by a four-point probe with an inter probe spacing s = 1.6 mm and needle probes with 20 μm diameter, which was connected to Keithley 2400 SMU with detection limit of 1GΩ (Keithley, UK). Sheet resistivity (or dc electrical conductivity, σ_{dc}) was calculated according to the formula, R_s (Ω•cm) = 4.532 V/I.t, where t the thickness (cm), V the voltage measured at the internal probes, and I the current applied to the external probes. Electrical contacts were made with colloidal silver paste (Ted Pella Inc. CA) and a Cu wire to connect with the SMU.

2.2.2. Force-volume spectroscopy

Force volume (FV) imaging is a characterization mode of scanning probe microscopy used to map force-deflection curves and intermolecular forces, which are correlated directly with successively acquired topography images. The analysis provides quantitative understanding and prediction of nanoscale chemical and mechanical properties. While it is easy to make qualitative comparison of mechanical properties across a sample, quantitative nanomechanical measurements with AFM require careful selection of probe along with calibration of the cantilever spring constant and tip radius described above. The cantilever stiffness *k* must broadly match that of the sample in order to have the appropriate level of sensitivity to probe the sample. Topographic and nanomechanical force-volume spectroscopy data were processed and analyzed using NanoScope Analysis software *ver.* 1.8 (Bruker Corp., Santa Barbara, CA) and/or designed algorithms, in PeakForce Quantitative Nanomechanical Mapping mode (PF-QNM) in ambient conditions, to determine the intermolecular force distribution between the tip and a surface, respectively. Traditional force-distance (*F-z*) curve data measures the force felt by the tip as it approaches and retracts from a point on the sample surface, while force volume is an array of force-distance curves over an extended range of sample area to generate force volume maps/images at the nanoscale, providing intermolecular force elasticity distribution maps that can be correlated with topography images [55,56,57], by means of fitting these curves with software in-built appropriate contact mechanics models such as JKR (Johnson-Kendall-Roberts) and DMT (Derjaguin-Müller-Toporov) for extracting quantitative nanomechanical properties including Young's modulus, stiffness and adhesion depending upon the heterostructures i.e., CD, GD, and DCD, respectively [58,59]. For our samples with spatial heterogeneity, it is necessary to acquire many data points to generate statistically significant quantitative values. All measurements were recorded at room temperature of 25 °C.

3. Results and discussion

3.1. Surface morphology

We characterized the constituent materials for their complex morphology and microstructure prior to conducting nanomechanical properties. Fig. 2a shows representative SEM images of MPACVD-grown diamond (D1), BCNW (C1), BCNW/Diam. (CD1), HFCVD-grown

Table 1
Summary of growth parameters for the samples under study.

Samples nomenclature	Sample description	Growth parameters	
		Diamond films	BCNW and rGO films /Overlayers
D1	Diam.$_{MPACVD}$ /*p*-Si(001)	MPACVD: 1%CH_4, 99%H_2, T_d: 700°C, P: 50 Torr, 1.3 kW, t_d: 6 h, d: 2 μm, [B/C] = 0 ppm, Total flow rate: 300 sccm	–
D2	Diam.$_{MPACVD}$/ SiO_2/*p*-Si(001)	MPACVD: 1%CH_4, 99%H_2, T_d: 700°C, P: 50 Torr, 1.3 kW, t_d: 5 h, d: 1.6 μm, [B/C] = 1.5–2 k ppm, Total flow rate: 300 sccm	–
CD1	BCNW/ Diam.$_{MPACVD}$/ SiO_2/*p*-Si(001)	–	8.5%CH_4, 90.5%H_2, 1%B_2H_6, T_d: 850 °C, P: 50 Torr, 1.3 kW, t_d: 40 min, d: 100 nm, [B/C] $_{gas\ phase}$ = 2 k ppm, Total flow rate: 328 sccm
D3$_{BDDh}$	B-doped Diam.$_{bot}$/*p*-Si (001)	MPACVD: 1%CH_4, 97%H_2, 2%B_2H_6, T_d: 700 °C, P: 50 Torr, 1.3 kW, t_d: 6 h, d: 1.52 μm, [B/C]$_{gas\ phase}$ = 4–5 k ppm, Total flow rate: 300 sccm	
CD2$_{BDDh}$	BCNW/B-doped Diam.$_{bot}$/*p*-Si (001)		8.5%CH_4, 90.5%H_2, 1%B_2H_6, T_d: 850 °C, P: 50 Torr, 1.3 kW, t_d: 40 min, d: 100 nm, [B/C] $_{gas\ phase}$ = 2 k ppm, Total flow rate: 328 sccm
D4$_{BDDl}$	B-doped Diam.$_{bot}$/*Fz*-Si (001)	MPACVD: 1%CH_4, 99%H_2, T_d: 700 °C, P: 50 Torr, 1.3 kW, t_d: 6 h, d: 2 μm, [B/C] = 1.5 k ppm, Total flow rate: 300 sccm	–
CD3$_{BDDl}$	BCNW/Diam.$_{bot}$ /*Fz*-Si(001)	–	8.5%CH_4, 90.5%H_2, 1%B_2H_6, T_d: 850 °C, P: 50 Torr, 1.3 kW, t_d: 40 min, d: 100 nm, [B/C]$_{gas\ phase}$ = 2 k ppm, Total flow rate: 328 sccm
DCD1	Diam.$_{top}$/ BCNW/ Diam.$_{bot}$/*Fz*-Si (001)	MPACVD: 1%CH_4, 99%H_2, T_d: 700 °C, P: 50 Torr, 1.3 kW, t_d: 4 h, d: 1.6 μm, [B/C] = 1.5 k ppm, Total flow rate: 300 sccm	–
D5$_{HFCVD}$	Diam.$_{HFCVD}$/*p*-Si (001)	HFCVD: 1%CH_4, 99%H_2, T_d: 700 °C, P: 20 Torr, t_d: 4 h, d: 1.95 μm, [B/C] = 0 ppm, Total flow rate: 300 sccm	–
GD1	rGO/Diam.$_{HFCVD}$ /*p*-Si(001)	HFCVD: 1%CH_4, 99%H_2, T_d: 700 °C, P: 20 Torr, t_d: 4 h, d: 2 μm, [B/C] = 0 ppm, Total flow rate: 300 sccm	rGO: 0.5 mg/mL GO coating followed by thermal reduction at 180 °C for 1 h, d: 25–30 nm

Note: T_d = deposition temperature, P = total chamber pressure, t_d = deposition time, d = film thickness.

diamond film (D5) and rGO/Diam. (GD1) samples revealing distinct surface morphology composed of uniformly dense packed well-faceted diamond crystallites. The diamond crystallites exhibit triangular growth habit or primarily ⟨111⟩ facets that start to turn into relatively smaller grains of same texture for B-doped diamond, while vertically aligned B-doped carbon nanowalls formed unique maze-like nanostructure, as well as complex BCNW layer intertwined with diamond surface as well as flat rGO nanosheets lying on rGO/Diam. specimens in covalent heterostructures, respectively. Corresponding representative cross-sectional SEM images are shown in Fig. 2a1 for diamond film, CD and DCD heterostructures yielding thickness of individual components of 1.5–2.0 ± 0.1 μm for diamond and 90 ± 10 nm for BCNW overlayers, respectively. The height of BCNW layer of 80–100 nm corresponds to film thickness of B-doped carbon nanowalls aggregate, while the lateral dimension varied between 30 and 50 nm. The open structure creates enhanced surface area accessible to electrolyte ion adsorption when the material used as an active electrochemical electrode or transducer for alternative energy and sensing. Likewise, Fig. 2b shows three-dimensional AFM images for quantification of grain size (d) and surface rms roughness (σ_{rms}), the analysis of which is shown in Fig. 2c, for all the samples studied in this work. The grain size varied between 0.40 and 0.55 μm and the surface roughness ranged from 110 to 125 nm for 2 μm thick bottom MPACVD grown diamond layer, which decreased marginally for higher B doping and upon BCNW deposition. Note that the grain size and surface roughness for HFCVD grown samples are larger (~0.9–1.1 μm and ~140–300 nm) than those growth with MPACVD.

3.2. Microstructure

The XRD profiles in Fig. 3a result from undoped diamond (D1), low B-doped diamond, D3$_{BDDl}$, BCNW only C1$_{BCNW}$, BCNW/Diam., (CD3) and rGO/Diam. (GD1) samples on Si(001) substrates in 2θ = 40°–90° range. The films show characteristic diffraction peaks assigned to polycrystalline diamond [(111) = 44°, (220) = 75°, and (311) = 92°] and carbon nanowalls [(002) = 22–26°] doped with substitutional boron atoms for the constituent layers, as well as the overlapped diffraction profiles along with Si substrates (004) = 69°. The X-ray diffracting domain or crystallite size of D3$_{BDDh}$, D4$_{BDDl}$ and D5$_{HFCVD}$ are calculated using Debye-Scherrer formula [60]:

$$L_{111\ (002)} = \frac{0.89\lambda}{\beta_{111\ (002)}\cos\theta_{111\ (002)}} \quad (1)$$

where λ (=1.54 Å) is the X-ray wavelength and $\beta_{111\ (002)}$ (in radian units) is the full width at half maximum (0.03–0.05°) of peaks. Qualitatively, the full width at half maximum (FWHM) of the characteristic XRD diamond peak becomes broader with boron and presence of a BCNW layer. In terms of average crystallite size, the un-doped diamond film crystallites of triangular (111) facets were marginally larger than those of low and high B-doped diamond (BDD$_{l/h}$) films of similar growth habits. Nevertheless, substitutional boron doping in diamond had the advantage of increasing the specific surface area and better conduction. Using Eq. (1), the crystallite size L_{111} turned out to be approximately 0.3 μm, which is lower than those evaluated from AFM, since this formulation is not applicable to larger grain size, which precludes those observed in most diamond films microstructure as for HFCVD in this work. In addition, the crystalline size along the *c* axis for BCNW is calculated to range between 15 and 18 nm and the interlayer spacing (L_c) between (002) graphene-like planes results in ~3.62 Å, indicative of high degree of graphitization. Also, it shifts toward higher 2θ values, indicating the development of compressive microstress in the films (see Table 2, residual internal stress) affecting the nanomechanical properties discussed in the following sections.

To enable technological applications mentioned above, specific sets of materials characteristics, requiring both microstructure and micro-

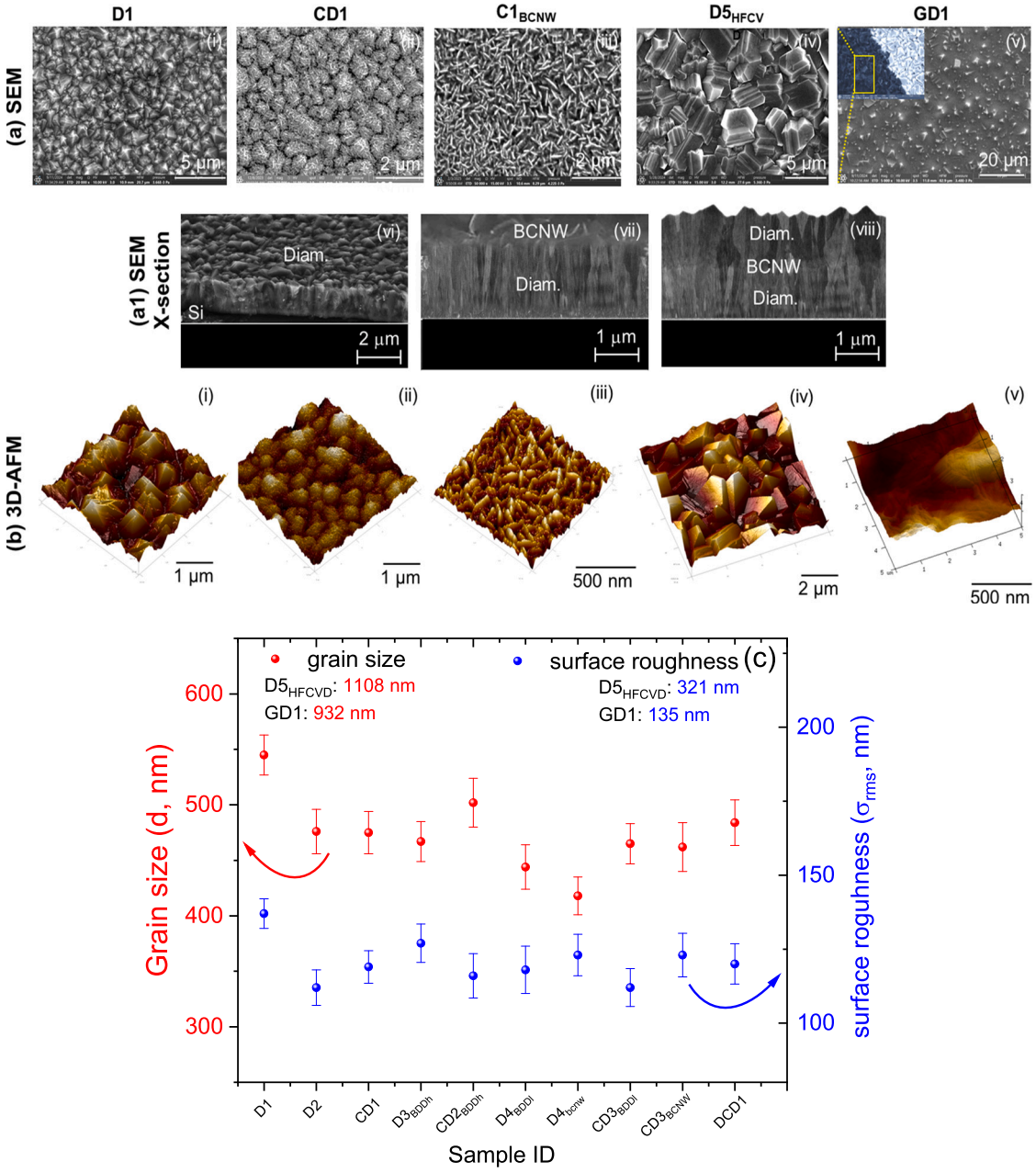

Fig. 2. Representative (a, a1) scanning electron micrographs (SEM) and cross-sectional images and (b) 3D-atomic force microscopy (3D-AFM) of polycrystalline diamond (undoped and B-doped D1 and D5), BCNW (C1), and corresponding hybrids (CD1 and GD1) revealing the surface morphology of constituents. (c) Variation of grain size (*d*, nm) and *rms* surface roughness (σ_{rms}, nm) for all the samples under study. Scale bars are shown at the bottom of the images.

stress/strain in diamond/graphene-like materials must be thoroughly determined. Raman micro-spectroscopy is typically used to characterize carbon-based materials since it is sensitive to local environments and different types of carbon-carbon bonding, polymorphism, and capable of monitoring changes in lattice vibrations for B-doped diamond and nanoscale BCNW and rGO. Raman spectroscopy is shown in Fig. 3b–c for undoped diamond (D1 and D5), BDD ($D3_{BDDh}$ and $D4_{BDDI}$), BCNW (C1), BCNW/BDD (CD1 and DCD1, BCNW region), and rGO/Diam. (GD1) samples helped to determine crystalline quality, diamond content (or sp^3 C fraction), and total stress. Qualitatively, they display characteristic signatures associated with diamond (sp^3 C), non-diamond (or sp^2 C), BCNW and rGO by themselves and as overlapped peaks when grown as overlayers on diamond films. The first-order Raman peak at 1332.5 cm^{-1} in diamond films attributed to zone-center phonon with full width at half maximum (FWHM; Γ) between 3.8 and 6.1 cm^{-1} for [B]/[C] =1.5–2 k ppm, while the broad band feature around 1500 cm^{-1} corresponds to non-diamond carbon due to grain boundaries and boron aggregates. Interesting to note that we did not observe asymmetric Fano line shape due to the fact B doping was much less than that required for Mott insulator to semiconductor or metallic transition in diamond [10,47]. The FWHM is a qualitative measure of crystalline quality of diamond and a broader peak characterizes the presence of defects/disorder. For BCNW and rGO, the spectra show prominent peaks characteristic of sp^2 C bonding including disorder-activated D band at ~1350 cm^{-1} (A_{1g} breathing mode or bent sp^2-carbon bonds) and the first-order graphitic G band at ~1588 cm^{-1} assigned to sp^2 C stretching mode (E_{2g}) [61], while BCNW/BDD and rGO/Diam. hybrid films show composite spectra with characteristic peaks associated with both the constituent layers. While there are various techniques for determining sp^3 C content such as electron energy loss spectroscopy, electron and neutron

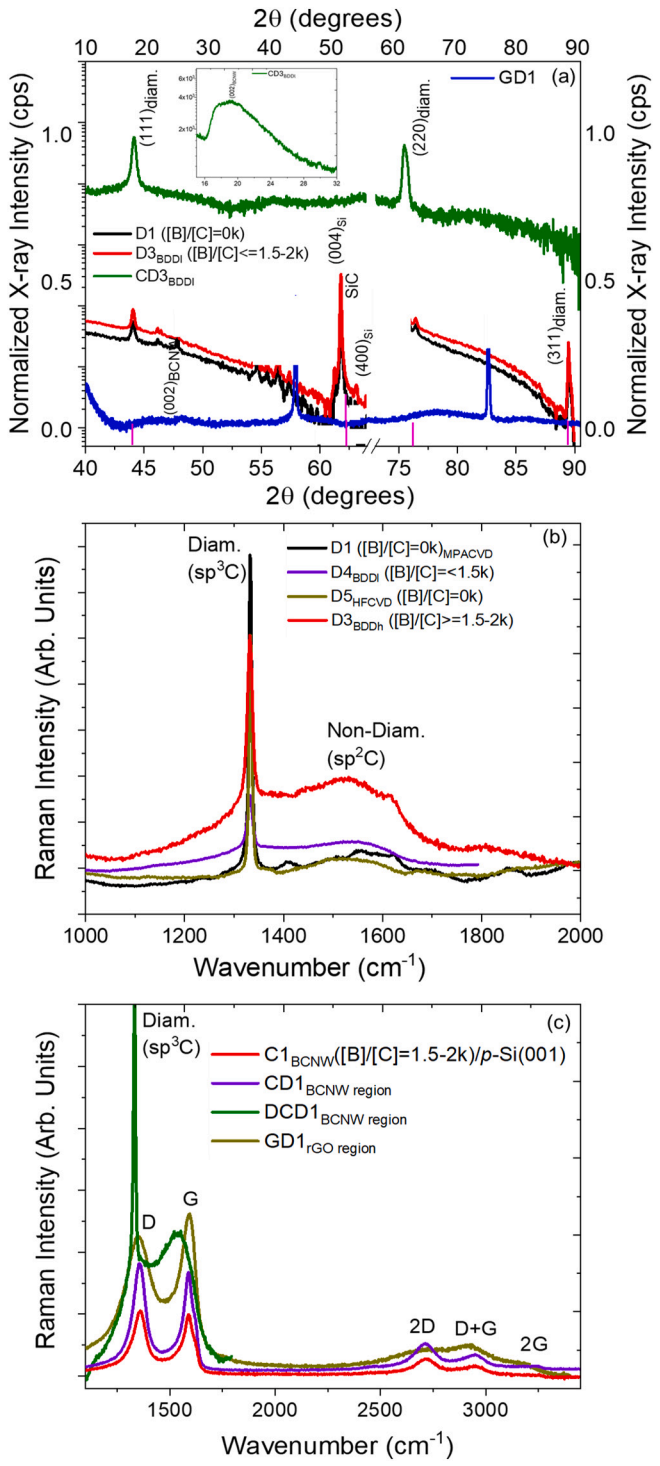

Fig. 3. (a) X-ray diffractograms (XRD) and (b, c) Raman spectra of undoped and B-doped polycrystalline diamond, BCNW, and corresponding hybrid films interfaces revealing the characteristic peaks associated with constituent layers.

diffraction, Raman spectroscopy was used to evaluate the diamond content using the following equation:

$$f_{sp3C}\ (\%) = (50 \times I_{Diam.}/50 \times I_{Diam.} + I_{non-Diam.}) \times 100 \quad (2)$$

where f is the ratio of the diamond peak area (integrated intensity) to that of the rest of the spectrum between 1100 and 1700 cm^{-1} (taking the Raman scattering cross-section of non-sp^3 bonded carbon to be 50 times that of diamond) [62]. Similarly, the microstress/strain is calculated

Table 2
Summary of diamond fraction and residual stress determined using XRD and Raman spectroscopy for the samples under study.

Samples nomenclature	Sample description	Microstructural properties		
		sp^3 C/sp^2 C (non-diamond) concentration (%)	Total stress -σ_{comp} (GPa)	Residual stress -σ_{int} (GPa)
D1	$Diam._{MPACVD}$/*p*-Si (001)	92–97/3–8	1.1–1.3	0.6–1.3
D2	$Diam._{MPACVD}$/SiO_2/*p*-Si (001)	90–94/6–10	1.3–1.5	0.7–1.2
CD1	BCNW/ $Diam._{MPACVD}$/SiO_2/*p*-Si (001)	75–80/20–25	0.8–1.1	0.4–1.1
$D3_{BDDh}$	B-doped $Diam._{bot}$ /*p*-Si(001)	92–95/5–8	0.7–1.3	0.5–0.9
$CD2_{BDDh}$	BCNW/B-doped $Diam._{bot}$/*p*-Si (001)	90–94/6–10	0.8–1.5	0.2–0.8
$D4_{BDDl}$	B-doped $Diam._{bot}$ /*Fz*-Si (001)	92–95/5–8	1.1–1.3	0.5–1.0
CD3	BCNW/B-doped $Diam._{bot}$ $Diam._{bot}$/*Fz*-Si (001)	70–80/20–30	1.3–1.6	0.6–1.1
DCD1	$Diam._{top}$/ BCNW/ $Diam._{bot}$/*Fz*-Si (001)	82–87/15–18	1.2–1.7	0.8–1.2
$D5_{HFCVD}$	$Diam._{HFCVD}$/*p*-Si (001)	95–97/3–5	1.2–1.4	0.3–0.8
GD1	rGO/ $Diam._{HFCVD}$/*p*-Si (001)	89–93/7–11	1.3–1.7	0.7–1.0

from the shift of Raman spectral band using the pressure coefficient of the diamond peak:

$$-1.9 \times \sigma_{comp}(GPa) = (\omega - \omega_0) \quad (3)$$

where $\omega_0 = 1332\ cm^{-1}$ for single crystal diamond [63]. Using Raman spectroscopic data, the sp^2 C cluster or domain size in the *a* axis (L_a) was calculated from the integrated intensity ratio of the D (I_D) and G peaks (I_G) following [61]:

$$L_a = \left(2.4 \times 10^{-10}\right) \times \lambda_L^4 \times \frac{I_D}{I_G} \quad (4)$$

where λ_L (=514 nm) is the laser excitation wavelength and L_a ranged between ~5.5–6.1 nm for BCNW and rGO samples. Next is the second-order Raman spectral features i.e., 2D peak centered at ~2690 cm^{-1} originating from zone-boundary K phonons. The other higher-order Raman bands include a combination (D + G) and second-order G (2G) bands occurring at ~2940 cm^{-1} and ~3200 cm^{-1}, respectively for BCNW and rGO related samples. Table 2 provides a summary of upper bound values of microstructural parameters from XRD and Raman spectroscopy.

It is likely there is a non-uniform distribution of boron and sp^2 C impurities in both the BDD and BCNW layers, which can affect the electrical and other physical properties and can create alternative conductive pathways which compete with through-grain conduction. Fig. 4 shows room temperature electrical *I-V* properties of all the samples studied in this work, reflective of weak semiconducting (non-ohmic) behavior predominated by the top layer. Moreover, since both the substrate and the films are p-type, we do not anticipate diode like behavior. Since the *I–V* is almost symmetric, the device is injection limited, in which the slope increased twice, indicating that the transport beyond a threshold is space charge limited in the presence of traps. The

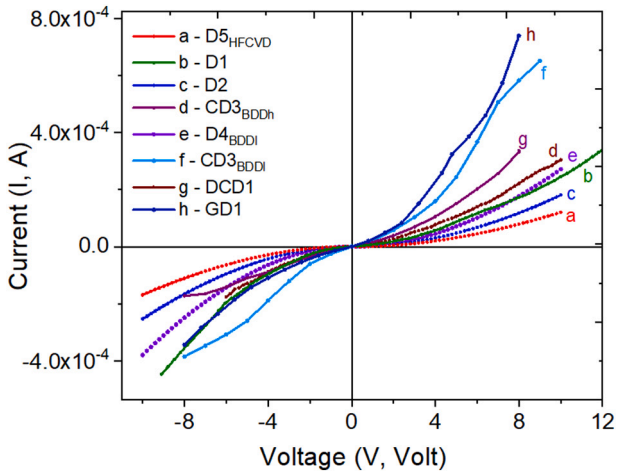

Fig. 4. Current versus voltage (*I-V*) plots for representative diamond films, and graphene-like BCNW and rGO and their hybrids exhibiting semiconducting (or non-ohmic) behavior.

electrical resistance calculated from the linear I-V regime gives rise to resistance $R_S\left(=\frac{\pi}{ln2}\frac{\Delta V}{I}\right)$ between 26 and 500 kΩ depending upon the B concentration in BDD and 2–4 kΩ for BCNW on BDD films. The corresponding room temperature electrical conductivity is determined using: $\sigma\ (=\frac{1}{R_S \times t})$, where *t* is the thickness, ranging between 0.01 and 0.19 S/cm and 2.5–1.2 S/cm (3.5–4.0 S/cm) for Diam. (D1 and $D5_{HFCVD}$), BDD ($D3_{BDDh}$ and $D4_{BDDl}$), BCNW/BDD (CD3), and rGO/Diam. (GD1) samples, respectively. Typically, there is less than full coverage of hydrogen-termination on the {110} oriented surface as compared to the {111} polycrystalline BDD surface. In addition, the nature of C—H bonds between BCNW and H-terminated diamond strongly influences the electronic character of the heterostructures, creating effective charge redistribution within the system consisting of regions of high electrical conductivity within a less conducting matrix, at least within the detection limit of >10 MΩ resistance.

3.3. Selective growth aspect of BCNW/BDD films

Vertical graphene (GNW) and carbon nanowalls (CNW) have gained significant attention due to their exceptionally high specific surface area (owing to their unique orientation, exposed shear edge planes, and non-stacking morphology), excellent electrical conductivity with B doping, scalability, and compatibility. Positioning them on insulating (undoped diamond) or semiconducting ($BDD_{l/h}$) diamond presents an excellent choice for various electroanalytical, optoelectronic, microelectronic, and thermal applications [12,13,64]. Herein we have grown vertically aligned BCNW on seeded Si(001) substrate and on diamond films grown in step 1 and thus the diamond surface acts as a nucleating layer. On a fundamental level of growth, BCNW are a self-organized network of vertical standing few-layer graphene grown on catalyst-free substrates which tended to have an induction period of 1–5 min depending upon the process conditions prior to onset of growth. Note that this induction period may decrease (<5 min) if the diamond surface is used as a base layer, which can catalyze the reaction [65,66]. Alternatively, the BCNW growth occurs directly from diamond by the use of boron admixed with nitrogen gas at higher deposition temperature inducing 2 × 1-reconstructed diamond (111) surface when the B doping density is adequate facilitating better adhesion and conformability at the interfaces. For BCNW growth by themselves on seeded Si substrates, it is speculated that at nucleation stage, the carbon species condense to form nano-islands of 2–5 nm size with the formation of dangling bonds. At these unsaturated bonds, carbon species start to form nanoflakes of smaller lateral dimension, leading to the growth of graphene-like nanosheets aligned along the microwave plasma electric field. Moreover, among these graphene sheets with random spatial orientation, those standing vertical to the substrate in most case grows relatively faster. The reactive carbon species arrive at the surface and with growth time, the vertical nanowalls meet with one another, eventually resulting in a maze by themselves and intertwined with underlying diamond (111) film. With further increase of growth time, it becomes challenging for the reactive carbon species to reach the sidewall, so that the wall thickness increase and then plateaus [67,68]. We also selectively deposited a diamond layer on top of BCNW/diam. (CD3) forming diam./BCNW/diam. (DCD1) covalent heterostructure for two-way registry that is not only graphene-on-diamond, but also diamond-on-graphene, where the sandwiched BCNW layer was preserved due to the seeding density too high and it protected the surface until a continuous layer of diamond was formed. One of the key aspects is such that in H-rich (and CH_x-rich) plasma, hydrogen abstraction on the growth surface is enhanced with boron and nitrogen admixture present in the gas phase which played a vital role in sp^3 to sp^2 transformation or local graphitization on diamond surface in contrast to H-poor and C_2-rich plasma as in acetylene, C_2H_2. It leads to a complex morphology with hierarchical features constituting polycrystalline diamond grains intertwined with vertically aligned BCNW thin layer, revealed via electron microscopy surface features and Raman spectral vibrational signatures. Based on experimental findings, a schematic diagram is provided (see Fig. 5a), that displays interfacial structures comprising vertical graphene-like BCNW and rGO layers aligned parallel to (111) diamond structure yielding local protruded ridges of the "wavy" or non-planarity of the sp^2-sp^3 carbon network and geometry interlocking at the interface corroborated with the high-resolution TEM image as in see Fig. 5b, also provided with the lattice spacing of diamond (0.208 nm) and graphene-like BCNW (0.36 nm). Subsequently, the graphene-like material adsorbed on diamond surface is a weak semiconductor with a finite gap depending on the surface adsorption due to variation of on-site energy induced by the (111) diamond surface, with the extra advantage of sustaining the characteristics of graphene-like overlayers, albeit with better adhesion influencing intermolecular forces. All these synthetic architectures comprising BCNW layers on BDD and oxygenated rGO layer (negatively charged) on diamond form covalent interfaces with H-terminated diamond (positively charged) surface [69], once again influencing nano-mechanics. The resulting material has high phase purity, controllable layer number, and good uniformity, which can be potentially used directly for high-performance devices requiring good thermal conductivity, as a viable platform for N/MEMS, sensing, and neuromorphic engineering [70,71].

3.4. Intermolecular force and nanomechanical property characterization

Following microstructure characterization, we now focus on evaluating the nanomechanical properties by way of atomic force microscopy and force volume spectroscopy. Density functional theory (DFT) calculations as well as experimental measurements (nanoindentation and uniaxial stress) suggest that the hardness and other mechanical properties of 'diamond-graphene' heterostructure may be superior to that of cubic diamond [72] thus motivating the usefulness of synthetic covalent heterostructures among natural carbon materials. Likewise, atomistic simulations predicted unusual mechanical properties of the diamond-graphene composite such as Young's modulus obtained by nano-indentation [73], which exceeded the stiffness of the original graphene film which are promising as wear and attrition resistant coatings [74,75]. However, the nanoindentation measurements are generally destructive in nature and therefore require non-destructive quantitative evaluation such as the use of scanning probe microscopy, uniquely capable of measuring nanomechanical properties at the nanoscale and quantify various intermolecular forces including Young's moduli, stiffness, and adhesion force between the tip and the samples' surface in force spectroscopy mode which provide a wealth of information about

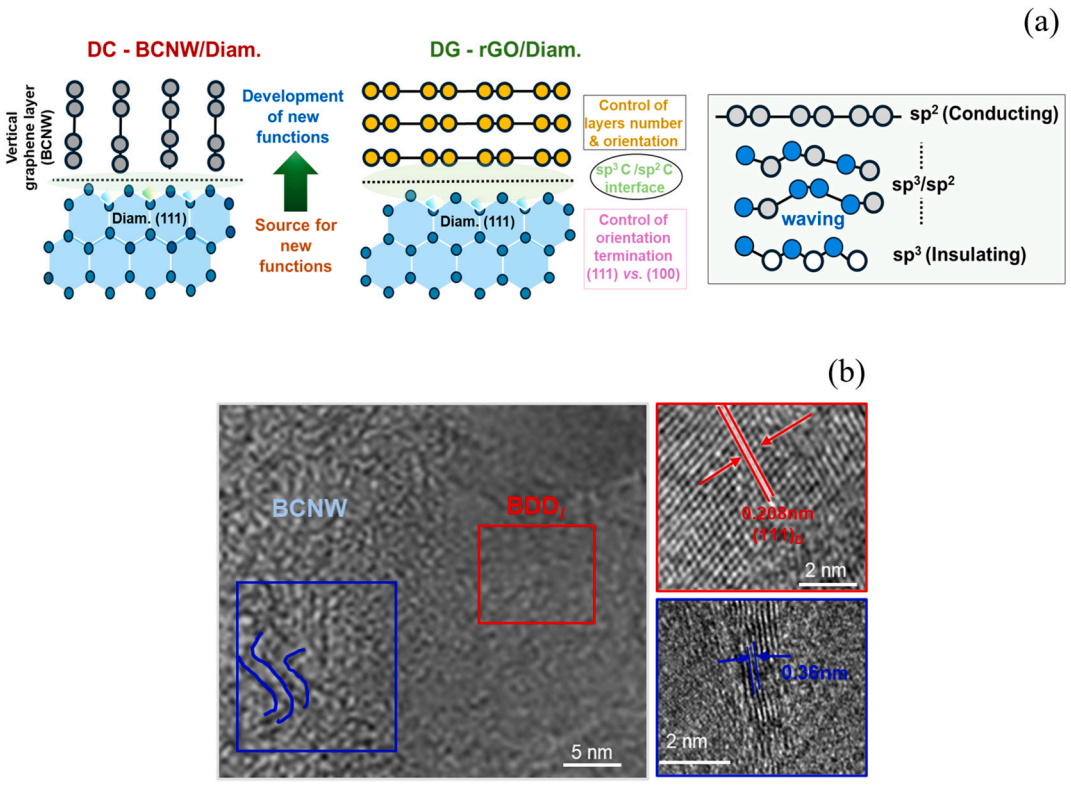

Fig. 5. (a) Schematic diagram of a concept for diamond (111) surface integrated with graphene-like vertically oriented BCNW layer and rGO (001) sheets aligned parallel to the plane of diamond film, both forming a "wavy" covalent interfacial structure. (b) Representative high-resolution TEM image of BCNW/diamond (BDD_l) interface showing waviness and lattice spacing for diamond and graphene-like BCNW constituents.

the chemical, mechanical strength, and electrostatic properties of surfaces [57,76,77].

The detailed schematic of the working principle of nanomechanical measurements using AFM force-distance cycle is shown in Fig. 6 (panel a). The measurements are conducted by recording the cantilever deflection as the tip approaches (blue curve) and retracts (red curve) a surface plotting a force curve as a function of displacement between tip and sample, used to deduce elastic moduli and mechanical stiffness. In addition, the force required to retract the AFM tip from the surface (hybrids and constituent films, herein) at that location and its shape is a measure of mechanical nature (stiffness; sharp and conical versus softness; diffuse and rounded) of the probed materials. In principle, the force volume (FV) imaging measures the distribution of such mechanical behavior over the topographic surface [78,79,80]. Mathematically, force F between tip and the sample is related to the cantilever's deflection that is fitted through the Hooke's (linear regime) law following:

$$F = k(\Delta z) = k.\alpha.V \tag{5}$$

where k is the cantilever's spring constant, α is the deflection sensitivity, and V is the measured deflection from millivolt to nanometers. The spring constant, k, determined by the geometry of tip following Euler-Bernoulli beam theory is given by [81]:

$$k = 2\pi^3 l^3 w \sqrt{\frac{\rho^3}{E}} f_0^3 \tag{6}$$

where l, w, f_0 and ρ are cantilever's length, width, fundamental resonance frequency and mass density, respectively, and E is Young's elastic modulus determined from one of the principal contact mechanics models such as Hertzian, JKR (Johnson-Kendall-Roberts) and DMT (Derjaguin-Muller-Toporov) depending upon the investigated surfaces (see Fig. 6, panels b–d). In terms of the AFM determined quantities, V, α, and f_0, the tip-sample force or adhesion force are given by:

$$F = 2\pi^3 l^3 w \sqrt{\frac{\rho^3}{E}} f_0^3 \alpha V \tag{7}$$

Also, since most surfaces grown using CVD deposition are heterogeneous, it is of interest to acquire a grid of force curves, so-called force volume imaging producing information about the spatial distribution of nanomechanical properties.

Fig. 7a–d show the force volume grids for MPACVD-grown D2, CD1, D4 and HFCVD-grown D5 samples grown on SiO_2/Si, *p*-Si and Fz-Si substrates, respectively, along with respective two-dimensional topography images, thereby providing important nanomechanical characterization capability that goes well beyond simple contrast. From the force-volume imaging and corresponding force-distance curves, at various points on the topographic surface marked with arrows (in the grid version) in Fig. 7a–d, the force maps are found to correlate with the surface morphology and spatial heterogeneity of surface and interface. Alternatively, un-doped diamond films deposited by both CVD methods have comparable inhomogeneity when deposited on Si(001) with an intrinsic SiO_2 layer in-between and it is further influenced by the presence of BCNW overlayer on diamond film depicting spatial inhomogeneity. As for the quantitative assessment of elasticity maps determined by fitting the *F-z* (force-displacement or deflection) curves with DMT model provided at various points as shown in Fig. 7, they depict relatively sharp (conical) behavior which becomes marginally rounded occasionally for BCNW/Diam. (CD1) sample and the model used is JKR. It is noteworthy that there is subtle difference among the mechanics models used to derive various parameters such that Hertz model neglects adhesion force F, the JKR model accounts for short-range adhesion within the contact area and model DMT considers long-range adhesion forces outside the contact area [58,59].

The upper bound values of 915 ± 35 GPa determined for diamond films which becomes 890 ± 12 GPa for BCNW/Diam. interface on grains having (111) texture, while for grain boundaries consisting of sp^2-rich C

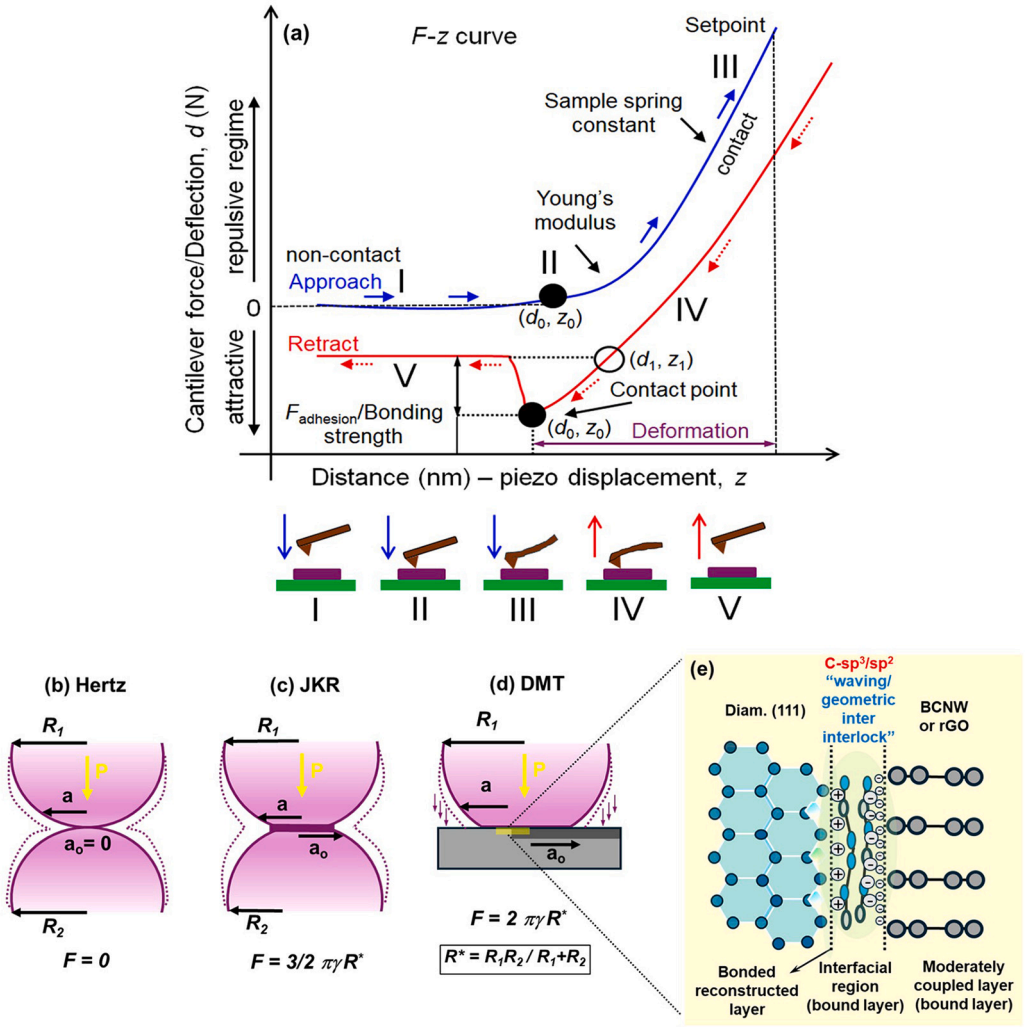

Fig. 6. (a) Profile of a force-distance (or *F-z* deflection) cycle measured with scanning probe microscope used for force spectroscopy, relating bonding and mechanical strength. The approach curve is highlighted in blue, and the retract curve is outlined in red. The black arrow indicates the jump-to-contact point where the tip snaps in to touch the surface. Schematic representation of relevant principal contact mechanics models used in AFM nano-mechanics: (b) Hertz, (c) JKR (Johnson-Kendall-Roberts) and (d) DMT (Derjaguin-Muller-Toporov). (e) a proposed three-layer model comprising bonded/restructured, interfacial bound and moderately bound top layer for the BCNW (and rGO)-diamond covalent heterostructures.

phase ranged between 360 and 598 ± 9 GPa. Nevertheless, these initial values suggest that the elasticity values for diamond grains are preserved post-BCNW deposition to a greater extent. Since force is the derivative of energy with respect to distance, the FV (Force-Volume) data were used to infer the potential energy between surfaces. Recalling Eq. (5), where *k* is the spring contact of the tip, we can estimate the contact force from the force plots by modeling the data. In all the polycrystalline diamond films, the interaction force seems to be largely dominated by strong adhesion, which is usually characterized by the sharp tip retract curve shape provided in the following section. In addition, it is also clear how the nature of substrate affects the upper bound values of elastic moduli affected by the intrinsic residual and compressive stress. For example, the Si(001) substrates with SiO_2 layer (D2) and float zone Si (001) ($D4_{BDDl}$) where the latter tended to have relatively lesser effective nucleation subsequently impacting the diamond film and have lower nanomechanical property values as compared to pristine *p*-Si(001) substrates grown films ($D3_{BDDh}$ and $CD2_{BDDh}$) which were the most reliable for colloidal nanodiamond nucleation (see Table 2).

The SEM, 2D- and 3D-AFM images shown in Fig. 8 are for a series of samples comprising lightly B-doped ($D4_{BDDl}$) bottom diamond layers, $C2_{BCNW}$, BCNW/Diam. (CD3) and Diam./BCNW/Diam. (DCD1) revealing surface morphology and displaying topography, along with a cross-section image (inset, SEM) determining thickness of bottom diamond film, while BCNW layer thickness was much smaller ranged between 80 and 90 nm abovementioned. The force-volume mapping was acquired and provided in Fig. 9a–f for the AFM topography as in Fig. 8. There is a distinct difference between the grain size and Young's modulus values for the bottom diamond layer for low B-doping versus no intentional doping. Qualitatively, while both diamond films show dense surface with uniform crystallites size, *albeit* smaller with B-doping on seeded Fz-Si(001) substrates, the upper bound for Young's modulus ranged between 908 ± 15 GPa (B-doped) to 913 ± 23 GPa (no or low B doping) on grains and 210–375 ± 13 GPa on disordered grain boundaries. It is noteworthy that for undoped bottom diamond layer grown on traditional *p*-Si(001) substrates shown in Fig. 7, the *E* values were higher (~1070 ± 20 GPa) when measured on grains despite both showing sharp conical force-distance retraction curves. The same holds true for BCNW/*Fz*-Si (C2) at 890 GPa when compared with (CD1) Fig. 7 at 900 GPa, which were grown on p-Si(001) substrates, the *E* values were lower as compared with the sample $D4_{BDDl}$ ranging between 348 and 913 ± 21 GPa depending upon the location on the nanowalls (lateral surface versus edge plane). This also indicates that these values lie along the underneath diamond layer showing reasonably good values as compared with those for D2 (Fig. 7a). Following these measurements,

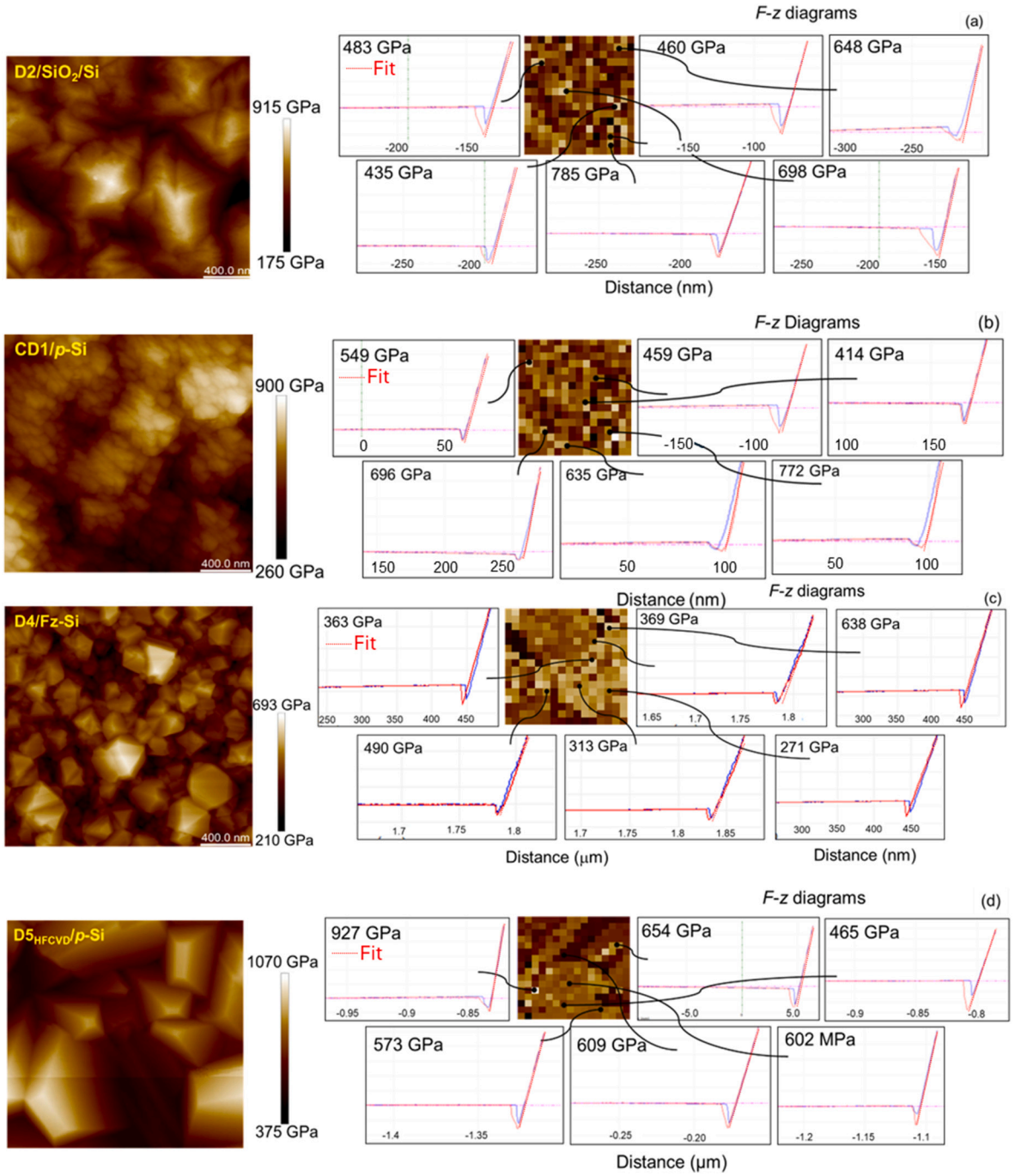

Fig. 7. Shown are force-volume elasticity distribution maps for (a) D2: MPACVD diamond (b) CD1: BCNW grown on BDD forming interface (c) D4 MPACVD diamond and (d) $D5_{HFCVD}$ diamond film, along with *F-z* curves marked at various points and 2D-AFM topography, measured using atomic force microscopy. Scale bar is at 5 μm.

we show similar force-volume mapping and force-deflection curves at several locations for the rest of the samples namely, BCNW/Diam. (CD3), Diam./BCNW/Diam. (DCD1, BCNW and top diamond layer regions) and rGO/Diam. (GD1, rGO region), since the top layers were selectively grown or deposited to develop various sp^2/sp^3 (vertical and lateral) interfaces. Qualitatively, the force-deflection (*F-z*) curves show marginal variation across the surface depending upon the location on diamond layer (grain or grain boundary), BCNW (edge or lateral site) and rGO (planar or folded sheet). Quantitatively, the distribution of upper bound *E* values ranged between 435–913 ± 48 GPa, 290–889 ± 29 GPa, 308–990 ± 41 GPa, and 310–995 ± 45 GPa for BCNW/Diam. (CD3), Diam./BCNW/Diam. (DCD1, BCNW region), Diam./BCNW/Diam. (DCD1, top Diam. region), and rGO/Diam., (GD1), respectively. This shows how deposition of every layer affects the *E* values for the subsequent layers as well as the role of functional groups, residual stress, geometric locking and composition (sp^3- versus sp^2-rich) in preserving their microstructure and functionality (see also Table 2). The E values were determined following JKR and DMT models depending upon whether the top layer is BCNW (presumably spherical shaped) versus diamond (presumably flatter rough surface), respectively. Nevertheless, the DMT model for adhesion is similar to that of JKR model; however, the resulting force equation uses the different constant, resulting in marginally higher values by 1.06 as compared to JKR model. The DMT model is a simple contact mechanics model for the interaction between a

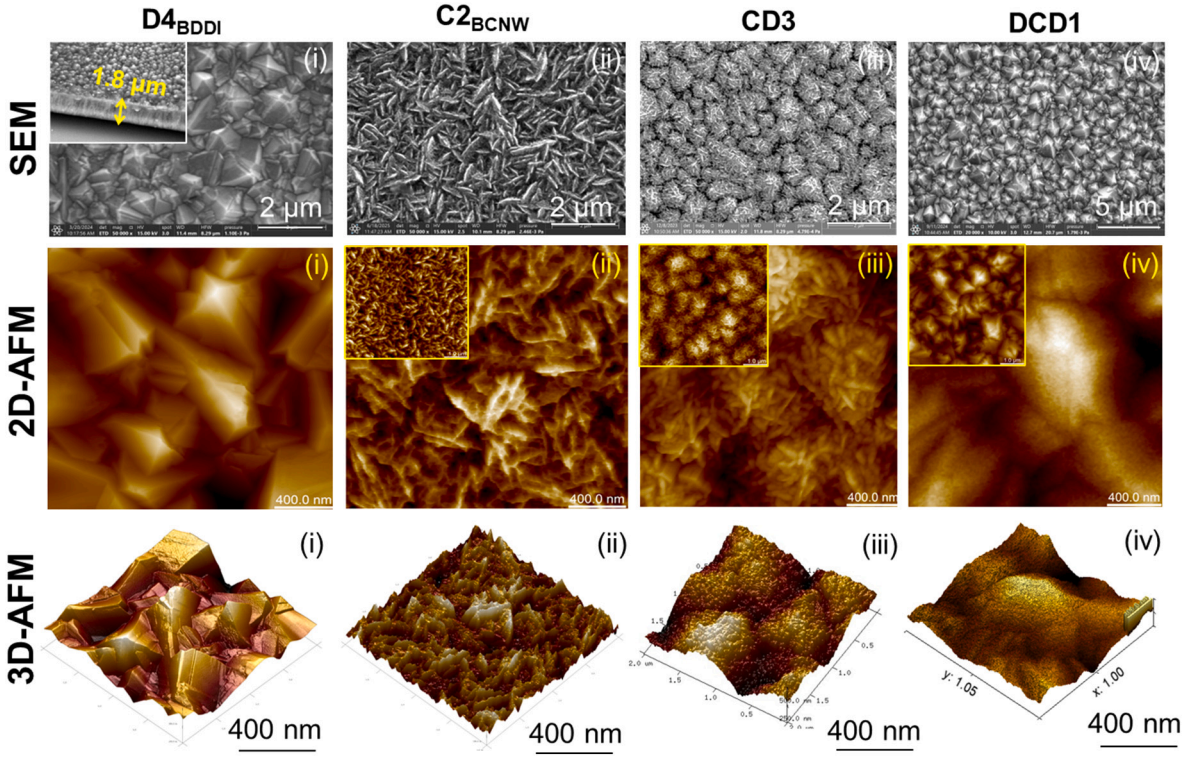

Fig. 8. Representative SEM, 2D-AFM, and 3D-AFM images of low B-doped polycrystalline diamond (D4), BCNW (C2), and corresponding hybrids (CD3 and DCD1) revealing the surface morphology of constituents and hybrid interfaces. Scale bars are shown at the bottom of the images.

hard (semiconductor) but compressible sphere and surface neglecting hysteretic adhesion forces. The parameter a_0, which corresponds to an interatomic distance, is used to achieve a continuous model for $F(z)$ (see Fig. 6). To mention, natural single crystal diamond and monolayer graphene Young's moduli are approximately similar (ca. ~1.0–1.1 TPa) [82,83]. Our experimentally determined values are comparable but smaller as anticipated due to the presence of grain boundaries sp^2C, B-doping, residual stress, while graphene-like layer suppresses the diamond wear by means of lubrication and damping effect which adds value for this novel class of covalent heterostructures in real-world application [84,85,86].

Though it is presumed that the elastic modulus values of polycrystalline diamond does not vary much with crystallite orientation, it is not correct, and to derive exact numbers for E, one must consider intrinsic anisotropy since CVD techniques grow randomly distributed polycrystalline grains namely, (111), (110) and (100) orientations. As per references [82, 87], to the first approximation the Hershey-Kröner-Eshelby averaging yields acceptable numbers with Poisson's ration $\nu = 0.079$ following $E/(1-\nu)$, which are compatible with those reported values for randomly oriented (111)-textured deposition. Moreover, the hydrogen terminated diamond strongly impacts the elastic behavior and appears to be responsible for the experimentally determined modulus observed in this and previous works along with BCNW (rGO)/diamond interface, where BCNW and rGO contains residual oxygenated functional groups.

Fig. 10 shows variation of mechanical stiffness (or spring constant, k) for all the samples studied at their respective positions on the samples surface. Depending upon the region, the interaction is dominated by adhesion force, usually characterized by shape of the retraction curves which indicates both stiffer (conical) and relatively softer (marginally round) behavior of the hybrids studied. The increase in k with the presence of BCNW and rGO interfaced with diamond is apparent as anticipated *albeit* marginal. It is worth mentioning that the ultimate k values are affected by unintentional post-processing condition of the preceding layer(s) and therefore careful control of processing conditions is equally important for rational design. From the view of electronic band structure, the all-carbon graphene-like/diamond interaction has been widely addressed with density functional theory (DFT) calculations and molecular dynamics (MD) simulations, which showed that *van der Waals* interactions dominate, and charge transfer depends upon the orientation of diamond crystallites. While no charge transfer occurs for (100) diamond, there is moderate charge transfer (p- or n-type) for the (111) diamond surface given the fact that graphene-like materials on <111> undoped diamond, B-doped and N-doped diamond preserving graphene's aromatic character practically for all terminations. DFT calculations also indicated little substrate interaction as conical intersection i.e., Dirac point preserved in monolayer graphene at the Fermi level. However, note that these calculations involved monolayer graphene-diamond interface for the sake of simplicity similar to electronic structure, but graphene-like BCNW and rGO suggest otherwise, and can affect the electrical properties at the interface because of geometric interlocking arising from lattice mismatch resulting in "wavy" interfacial structure. These heterostructures offers excellent current-carrying abilities, while creating effective charge redistribution within the system. Similarly, the increasing elastic moduli and mechanical strength are comparable to those experiments conducted using nanoindentation supported with theoretical DFT calculations and MD simulations [88,89], which was quite encouraging. The studied systems consist of carbon networks that tend to have multiple conduction pathways useful for rapid ion transportation and mechanical robustness for BCNW, rGO and diamond layers effective for heat dissipation, desirable for electrochemical sensing and thermal management, respectively. The performance also depended upon the diamond surface termination (—H and —O), where our samples are part H- and part O-terminated given the fact the (110) surface also have a tendency to oxidize besides (111) surface in ambient conditions.

3.5. *Surface-dependent adhesion properties characterization*

Since the physical (electrical and mechanical) performance of a

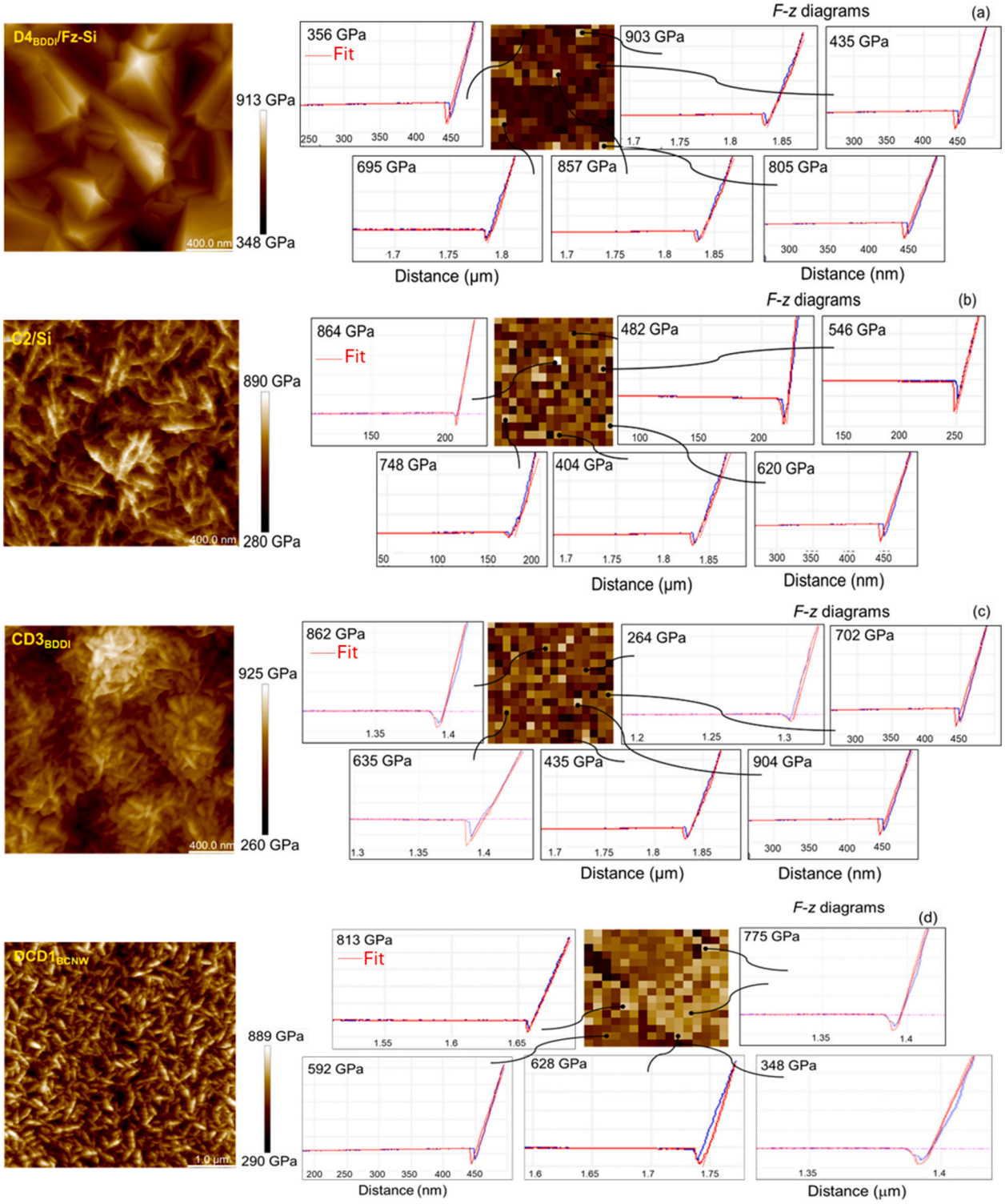

Fig. 9. Shown are force-volume elasticity distribution maps for (a) low B-doped polycrystalline diamond ($D4_{BDDI}$), (b) BCNW (C2), (c–f) hybrids ($CD3_{BDDI}$, DCD1-top diamond and BCNW regions, and GD1) forming interfaces, along with *F-z* curves marked at various points and 2D-AFM topography, measured using atomic force microscopy. Scale bar for all is at 5 μm.

graphene–diamond heterostructure is sensitively influenced by the adhesion intensity, our analysis provides insights into the design and development of graphene–diamond multifunctional hybrid nano-devices. Graphene and graphene-like material adhesion studies have rarely focused on the diamond lattice thus their adhesion properties remain elusive. Moreover, attempts are mainly focused on pristine monolayer graphene with theoretically smooth substrates, which is not the case for our polycrystalline diamond (surface roughness ranged between 100 and 300 nm, see Fig. 2c). Therefore, the poly-/micro-diamond rough surface is more in tune with the real-world applications, and understanding of graphene-like BCNW and rGO on diamond is significant. This pioneer attempt in determining adhesion force from

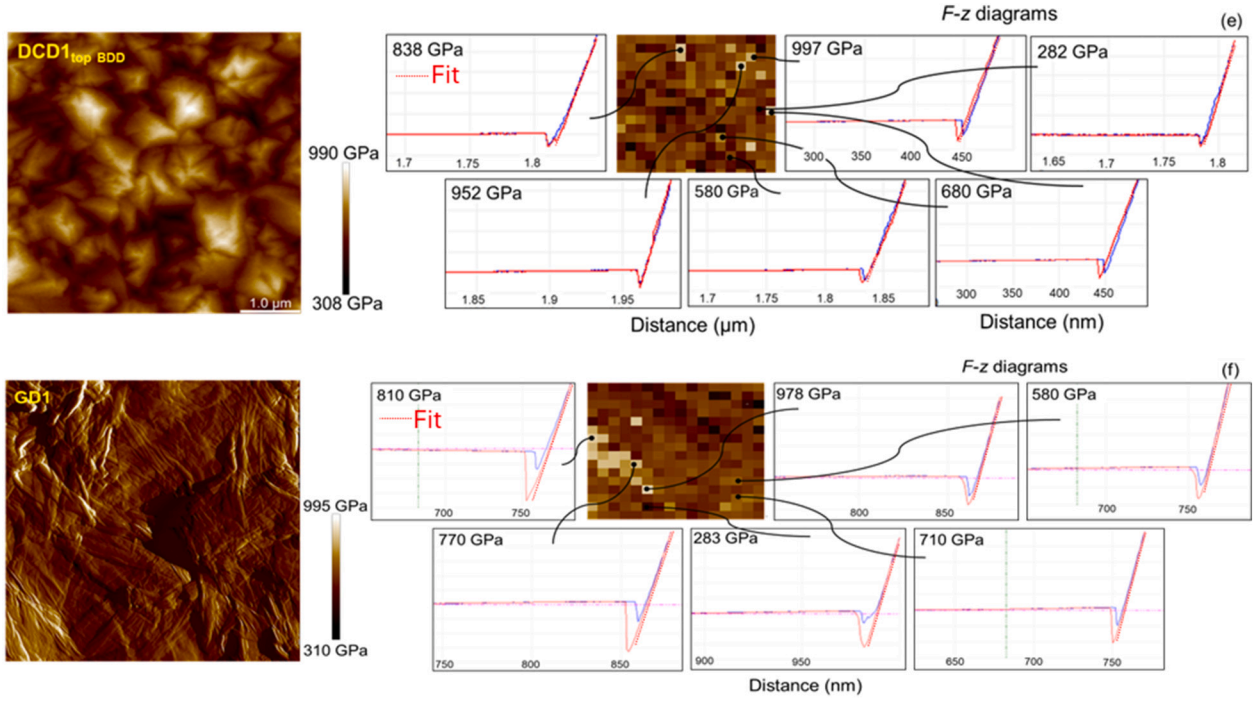

Fig. 9. (*continued*).

experiments provide insights and enhance our understanding complemented with the reported investigations [82,83]. It is worthwhile to mention that DFT and MD alone cannot address the inherent dynamics of adhesion intensity. Nevertheless, despite the use of diamond for binding monolayer graphene, the intrinsic properties of graphene and the related materials can be strongly influenced by crystal orientation [(111), (110)], extrinsic surface morphology including corrugations yielding to surface roughness, and terminating species (H, O, and OH), which subsequently affect adhesion performance, electronic properties, and interfacial thermal resistance of the heterostructures.

Here we determined surface-dependent adhesion force intensity values for some of our representative heterostructure samples. As the tip makes mechanical contact with the surface it may adheres to the sample due to local attractive forces, and the adhesion force is described as the force required by tip to retract away also measured through force spectroscopy. The individual force-deflection (*F-z*) curves correspond to the approach/retract force curves showing minimal adhesion dip (marked by solid black circle in Fig. 6a) as the tip retracts from the surface. Therefore, force versus tip-sample separation measurements plots are used to extract adhesion force following the Derjaguin-Muller-Toporov (DMT) and Johnson-Kendall-Roberts (JKR) elastic adhesive contact mechanics models described above, linked to sliding friction coefficient [58,90]. Adhesion force maps were generated for representative samples from *F-z* curves (16 × 16 FV mapping grid) obtained with silicon nanoprobes at an applied force of 1nN for areas measuring 2 × 2 μm^2 and the extracted values and range are shown in Fig. 10b and c. The histogram of the measurements for DCD1 ($Diam._{top}$) sample and equivalent $D4_{BDDl}$ ($DCD1_{bottom}$) and CD3 ($DCD1_{BCNW}$) samples (Fig. 10d) exhibited a bimodal adhesion intensity distribution with two prominent peaks at 0.1 ± 0.07 nN (first peak) and 0.3 ± 0.07 nN (second peak) along with other samples for which the upper bound was 0.45 ± 0.08 nN for GD1 (rGO/Diam.) sample. It has been reported that graphene-diamond covalent heterostructures interact through weaker van der Waals interaction forces and feature homogeneous covalent bonded interface seamlessly extend from diamond (111) sp^3 C to sp^2 C [vertical BCNW and rGO (0001) nanosheets] through geometric interlocking (see Fig. 5) [35]. The covalent carbon networks are expected to be robust enough to address high-power electronics and ultrahard mechanical machining and wear resistant protective coatings. These results are unprecedented and provide useful insights into the interfaces of exotic C sp^2/sp^3 and sp^3/sp^2 interphases. However, the adhesion between graphene and the ideal diamond (111) facet is still thought of as weaker binding since it is significantly lower than that on nickel and iron [91,92]. Nevertheless, as the diamond (111) has also been applied in previous experimental studies [93], the diamond (111) facet is recommended for the fabrication of the graphene–diamond heterostructure owing to its relatively high interfacial adhesion strength [85]. Thus, these studies suggest there is a delicate competition among the interfacial friction, adhesion strength, and the bending stiffness of constituent thin films.

Therefore, it is conceivable adhesive properties are not only closely related to intrinsic properties of the individual phases of constituent layers, but more so to the boundary conditions across the hetero-interfacial interphases. Furthermore, the interfacial volume fraction of carbons for graphene-like materials is substantially large compared with diamond. Thus, the interfaces are the dominant features of hybrids leading to surface hybridization, restructuring of the interfacial carbon atoms providing stability and two-way communication for DCD structure. There are at least two characteristics critical for describing interfaces, namely, principal contact mechanics models and interfacial bonding distribution. For the first, Fig. 6 shows a schematic of relevant principal contact mechanics models including Hertz, JKR, and DMT, with a fundamental difference how these models treat contact radius and adhesion forces between two surfaces which are shown as elastic spheres (AFM tip) and a flat surface (sample). While Hertz model neglect adhesion force F, the JKR model accounts for short-range adhesion for CD structure and DMT model takes into consideration of long-range adhesion force outside the contact area such as for DCD and GD structures. Tanaka et al. [94] also proposed a multilayer model that was applied for graphene-polymer interfaces [31] and now extended for graphene-like/diamond covalent heterointerfaces comprising bonded, bound and moderately bound layers, shown in Fig. 6e. The first bonded layer is strongly bonded by covalent and C—H bonds or van der Waals forces, to both nanomaterials (BCNW and rGO) and underneath diamond layer. The second bound layer is an interfacial region consisting of a deformed "waving" layer strongly bound to or interacting with the

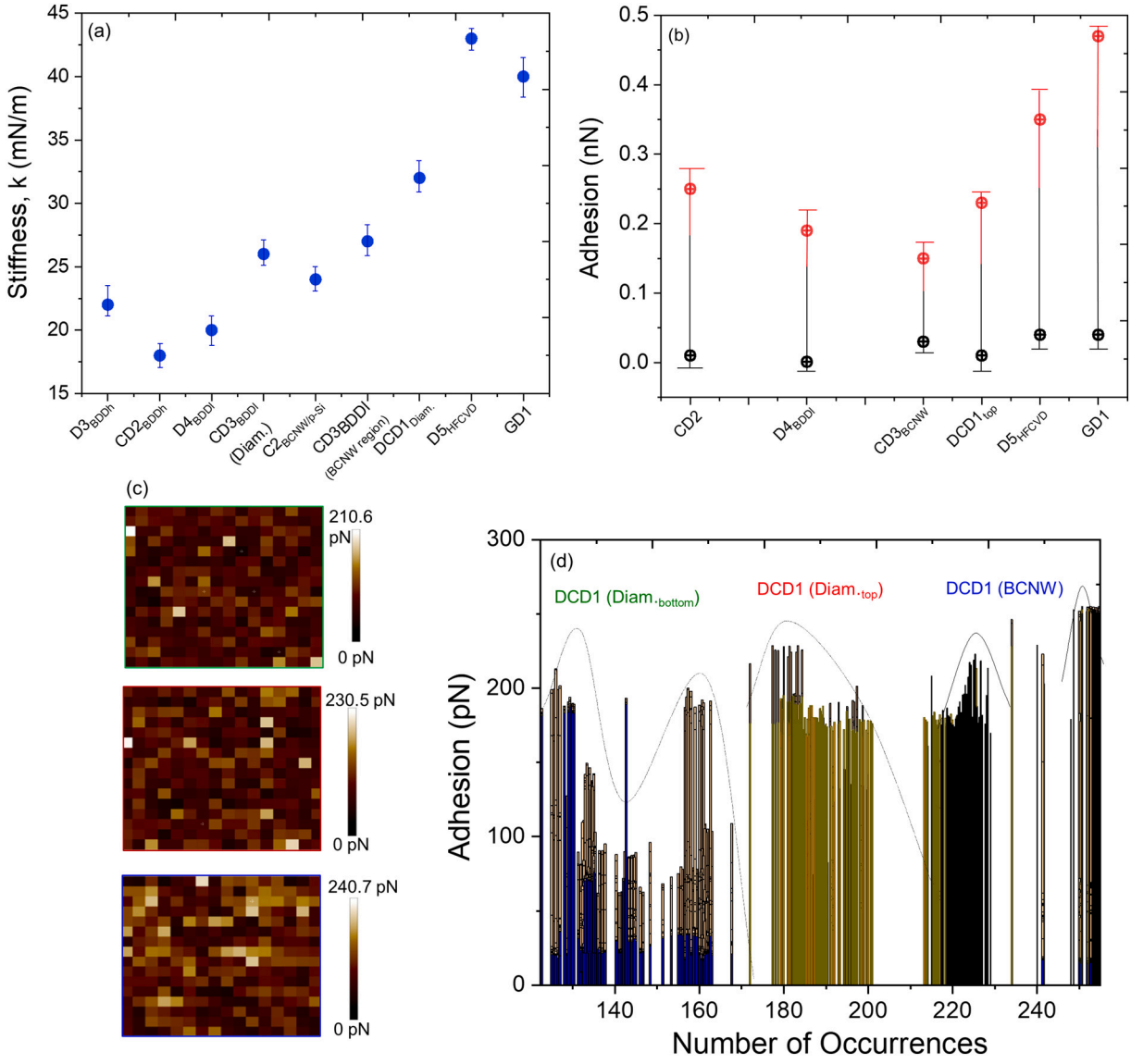

Fig. 10. Variation of (a) stiffness constant, *k* for samples under study (b) adhesion range for representative samples (c) adhesion distribution maps and (d) adhesion histograms for $D4_{BDDI}$, $CD3_{BDDI}$, and DCD1 samples.

bonded layer and the surface of the nanomaterials. The third layer is moderately coupled and interacting with the second layer which differs from that of bulk diamond. In addition to the bonding, the topography of the interface layer is also strongly affected by the surface termination and hybridization as well as attractive charge distribution. Within these regions, van der Waals force (moderate range) is involved and can alter the interfacial layers and thus a wide range of measured *E*, *k*, and adhesion force values driven by overlayers with defects (e.g., conducive Stone-Wales defects to enhancing adhesion strength) and enabling suppression of conversion of rough diamond surface to amorphous sp^2 C, dangling C atoms, and single C atoms. These protocols with force spectroscopy mode can be applied to a broad range of materials and molecular systems to gain fundamental insights into chemical and mechanical properties. Thus, the key benefits are the capabilities for correlating force measurements with specific features of AFM topography frames for unraveling the roles of microstructure and function at small size scales.

4. Conclusion

The novel diamond-graphene-like covalent heterostructures provide a basis of revolutionary applications for “all carbon” systems. However, to effectively utilize these structures, understanding and interrelating their structural and physical properties (nanomechanical, in particular) become indispensable. We reported a systematic growth of various covalent heterostructures including graphene-like carbon nanowalls-on-diamond and diamond-on-graphene-like carbon nanowalls sandwiched between diamond layer and characterized using XRD, Raman spectroscopy, atomic force microscopy and force spectroscopy to determine microstructure, residual stress, spatial distribution of carbon bonding, and various intermolecular forces, respectively. We elucidated the effects of boron doping and substrate upon the physical properties besides films microstructure. Three specific features–Young's modulus, spring constant and adhesion–extracted from force spectroscopy are established as pivotal nanomechanical properties. The surface structure in both the undoped and doped diamond films has a strong effect on intermolecular forces and surface-dependent adhesion properties. Meanwhile, information in force volume decoupled from topographic data, and the Young's moduli and mechanical strength (stiffness) estimated using principal contact mechanics models depending upon the top layer that followed: $rGO/Diam._{HFCVD} \geq$ Diam./BCNW/Diam. > BCNW/BDD $\geq$ Diam./*p*-Si(001) order. The findings are discussed in

terms of surface, microstructure properties (residual stress, composition, geometry interlocking and interfacial interactions) and restructuring of interfacial carbon atoms, providing stability of the resulting covalent configurations. The diamond/BCNW/diamond structures also ensure two-way registry by means of diamond-on-carbon nanowalls and carbon nanowalls-on-diamond such that it will provide additional interlocking, charge transport, and stability.

Features within the topography correlated with force-volume mapping helped to establish *microstructure-property* interrelationships at the nanoscale spatial resolution. The primary reason for reasonable mechanical properties is due to surface reconstruction of diamond and geometric interlocking of carbon networks to enhance interfacial interactions and appearance of mesoscopic structures at the interface. The presumable rather weaker interaction between the two allotropic carbons restricted for monolayer graphene on single crystal diamond (ideal case), but these covalent carbon hybrid systems studied here determine unique mechanical performance, thanks to sliding-induced graphitization and/or passivation of dangling bonds promoting geometric interlocking. Thus, the interphases at the interfaces become responsible for outstanding nanomechanical and good adhesion (or alternatively friction) properties. We also attempted to discuss our findings in terms of interfacial polarization, reminiscent of an electric double-layer model due to positively charged H-term. Diamond and negatively charged oxygenated BCNW/rGO overlayers. These results are promising for diverse technologies and underscore their universal applicability, rapidity, and non-destructive nature.

CRediT authorship contribution statement

Sanju Gupta: Writing – review & editing, Writing – original draft, Visualization, Resources, Project administration, Methodology, Investigation, Funding acquisition, Formal analysis, Data curation, Conceptualization. **Katarzyna Bury:** Writing – review & editing, Visualization, Validation, Software, Resources, Formal analysis, Data curation. **Paul W. May:** Writing – review & editing, Validation, Resources, Investigation.

Declaration of competing interest

The authors declare that they have no known competing financial interests or personal relationships that could have appeared to influence the work reported in this paper.

Acknowledgements

The corresponding author (S.G.) gratefully acknowledges financial support for these studies from Gdansk University of Technology by the DEC-37/2022/IDUB/1.1/NOBELIUM grant under IDUB Nobelium Joining Gdańsk Tech Research Community - 'Excellence Initiative - Research University' program. The authors also thank the following for help with sample deposition (R. Bogdanowicz, Gdańsk University of Technology), SEM (M., Narajcyzk, Faculty of Biology, University of Gdańsk), XRD (M. Gazda, Institute of Nanotechnology and Materials Science, Gdańsk University of Technology), and RS (M. Sawczak, Polish Academy of Sciences-Gdańsk). We are also thankful to all the reviewers for their valuable feedback which improved the manuscript.

Data availability

Data will be made available on request.

References

[1] P.L. Walker (Ed.), Chemistry and Physics of Carbon: A Series of Advances Vol. 16, CRC Press, (Wiley Online Library), 2021, p. 336.
[2] J.E. Field, The Properties of Natural and Synthetic Diamond, Academic Press, London, 1992.
[3] H.W. Kroto, J.R. Heath, S.C. Obrien, et al., C_{60} Buckminsterfullerene, Nature 318 (6042) (1985) 162–163.
[4] S. Iijima, Helical microtubules of graphitic carbon, Nature 354 (6348) (1991) 56–58.
[5] A.K. Geim, K.S. Novoselov, The rise of graphene, Nat. Mater. 6 (2007) 183–187.
[6] J.C. Angus, P. Koidl, S. Domitz, in: J. Mort, F. Jansen (Eds.), Plasma Deposited Thin Films, CRC, Boca Raton, FL, 1986.
[7] C.J.H. Wort, R.S. Balmer, Diamond as an electronic material, Mater. Today 11 (2008) 22–28.
[8] V.D. Blank, V.D. Churkin, B.A. Kulnitskiy, I.A. Perezhogin, A.N. Kirichenko, V. N. Denisov, S.V. Erohin, P.B. Sorokin, M.Y. Popov, Phase diagram of carbon and the factors limiting the quantity and size of natural diamonds, Nanotechnology 29 (2018) 115603.
[9] P.W. May, Diamond thin films: a 21st century material, Philos. Trans. R. Soc. Lond. Ser. A Math. Phys. Eng. Sci. 358 (2000) 473–495.
[10] R. Zulkharnay, P.W. May, Applications of diamond films: a review, Funct. Diamond 4 (2024) 241060.
[11] C.E. Bradley, J. Randall, M.H. Abobeih, R.C. Berrevoets, M.J. Degen, M.A. Bakker, M. Markham, D.J. Twitchen, T.H. Taminiau, A ten-qubit solid-state spin register with quantum memory up to one minute, Phys. Rev. X 9 (2019) 031045.
[12] S. Gupta, M. Sawczak, M. Narajczyk, K. Bury, R. Bogdanowicz, Development of opto-electronic synapses based on graphene-like (sp^2C)/diamond (sp^3C) heterojunctions as "all carbon" ReRAM devices for neuromorphic computing, APL Electronic Devices 2 (2026) 016111-1–016111-26.
[13] M. Sobaszek, K. Siuzdak, J. Ryl, M. Sawczak, S. Gupta, S.B. Carrizosa, M. Ficek, B. Dec, K. Darowicki, Bogdanowicz., Diamond phase (sp^3-C) rich boron-doped carbon nanowalls (sp^2-C): physicochemical and electrochemical properties, J. Phys. Chem. C 121 (38) (2017) 20821–20833.
[14] E. Bertran-Serra, S. Rodriguez-Miguel, Z. Li, Y. Ma, G. Farid, S. Chaitoglou, R. Amade, R. Ospina, J.L. Andújar, Advancements in plasma-enhanced chemical vapor deposition for producing vertical graphene nanowalls, Nanomaterials 13 (18) (2023) 2533.
[15] S. Gupta, M. Narajczyk, M. Sawczak, J.B. Jasinski, R. Bogdanowicz, S. Yang, Flexible MXene/laser-induced porous graphene asymmetric supercapacitors: enhanced energy density of lateral and sandwich architectures under different electrolytes, Small 21 (20) (2025) 2502297.
[16] S. Gupta, S.B. Carrizosa, B. McDonald, J. Jasinski, N. Dimakis, Graphene-family nanomaterials assembled with cobalt oxides and cobalt nanoparticles as hybrid supercapacitive electrodes and enzymeless glucose detection platforms, J. Mater. Res. 32 (2017) 301–322.
[17] S. Gupta, M. Narajczyk, M. Sawczak, R. Bogdanowicz, Perspectives on electron transfer kinetics across graphene-family nanomaterials and interplay of electronic structure with defects and quantum capacitance, Sci. Rep. 15 (1) (2024) 19722, https://doi.org/10.1038/s41598-025-04357-x.
[18] J. Miller, Perspective on electrochemical capacitor energy storage, Appl. Surf. Sci. 460 (2018) 3–7.
[19] S. Gupta, A. Sharits, J. Boeckl, Quantitative morphometry of topological graphene-based aerogels and carbon foams by X-ray micro-computed tomography, J. Appl. Phys. 134 (2021) 074902:1–074902:12 [Cover Page].
[20] S. Gupta, N. Dimakis, Elucidating the effects of oxygen- and nitrogen-containing functional groups in graphene nanomaterials for applied electrochemistry by density functional theory, J. Appl. Phys. 130 (2016) 084902:1–084902:19.
[21] W. Hummers, R.J. Offeman, Preparation of graphitic oxide, Am. Chem. Soc. 80 (1958) 1339.
[22] J. Vejpravová, Mixed sp^2-sp^3 nanocarbon materials: a status quo review, Nanomaterial 11 (2021) 2469:1–2469:28.
[23] Q. Yuan, C.T. Lin, K.W.A. Chee, All-carbon devices based on sp^2-on-sp^3 configuration, APL Mater. 7 (2019) 030901.
[24] E.H.L. Falcao, F. Wudl, Carbon allotropes: beyond graphite and diamond, J. Chem. Technol. Biotechnol. 82 (6) (2007) 524–531, https://doi.org/10.1002/jctb.1693.
[25] S.J. Kamatchi, T.H. Chang, S.K. Bikkarolla, S.S. Roy, P. Papakonstantinou, S. Drijkoningen, P. Pobedinskas, M. Van Bael, N.H. Tai, I.N. Lin, K. Haenen, Growth, structural, and plasma illumination properties of nanocrystalline diamond-decorated graphene nanoflakes, RSC Adv. 6 (68) (2016) 63178–63184.
[26] Y. Tzeng, W.L. Chen, C.H. Wu, J.Y. Lo, C.Y. Li, The synthesis of graphene nanowalls on a diamond film on a silicon substrate by direct-current plasma chemical vapor deposition, Carbon 53 (2013) 120–129.
[27] B. Li, B.K. Liu, L.K. Tong, Z. Zhao, Y. Tian, Discovery of gradia between graphite and diamond, Acc. Mater. Res. 5 (5) (2024) 614–624.
[28] P. Nemeth, K. McColl, R.L. Smith, M. Murri, L.A.J. Garvie, M. Alvaro, B. Pecz, A. P. Jones, F. Cora, C.G. Salzmann, et al., Diamond-graphene composite nanostructures, Nano Lett. 20 (2020) 3611–3619.
[29] F. Bundy, Direct conversion of graphite to diamond in static pressure apparatus, J. Chem. Phys. 38 (3) (1963) 631–643.
[30] T. Nakajima, A. Mabuchi, R. Hagiwara, A new structure model of graphite oxide, Carbon 26 (1988) 357–361.
[31] S. Gupta, B. McDonald, S.B. Carrizosa, C. Price, Microstructure, residual stress, and intermolecular force distribution maps of graphene/polymer hybrid composites: nanoscale morphology-promoted synergistic effects, Compos. Part B 92 (2016) 175–192.
[32] S.N. Zhao, K. Larsson, First principle study of the attachment of graphene onto non-doped and doped diamond (111), Diam. Relat. Mater. 66 (2016) 52–60.
[33] W. Hu, Z.Y. Li, J.L. Yang, Diamond as an inert substrate of graphene, J. Chem. Phys. 138 (2013).

[34] L.Y. Antipina, P.B. Sorokin, Converting chemically functionalized few-layer graphene to diamond films: a computational study, J. Phys. Chem. C 119 (2015) 2828–2836.
[35] B.P. Reed, M.E. Bathen, J.W.R. Ash, C.J. Meara, A.A. Zakharov, J.P. Goss, J. W. Wells, D.A. Evans, S.P. Cooil, Diamond (111) surface reconstruction and epitaxial graphene interface, Phys. Rev. B 105 (2022) 205304.
[36] E. Luais, M. Boujtita, A. Gohier, A. Tailleur, S. Casimirius, M.A. Djouadi, A. Granier, P.Y. Tessier, Carbon nanowalls as material for electrochemical transducers, Appl. Phys. Lett. 95 (2009) 014104.
[37] M. Hiramatsu, M. Hori, Carbon Nanowalls, Springer, Vienna, 2010.
[38] T.C. Hung, C.F. Chen, W.T. Whang, Deposition of carbon nanowall flowers on two-dimensional sheet for electrochemical capacitor application, Electrochem. Solid-State Lett. 12 (2009) K41–K44, https://doi.org/10.1149/1.3099325.
[39] E. Stratakis, R. Giorgi, M. Barberoglou, T. Dikonimos, E. Salernitano, N. Lisi, E. Kymakis, Three-dimensional carbon nanowall field emission arrays, Appl. Phys. Lett. 96 (2010) 043110, https://doi.org/10.1063/1.3298648.
[40] P.J. Hall, M. Mirzaeian, S.I. Fletcher, F.B. Sillars, A.J.R. Rennie, G.O. ShittaBey, G. Wilson, C.R. Cruden, Energy storage in electrochemical capacitors: designing functional materials to improve performance, Energy Environ. Sci. 3 (2010) 1238–1251.
[41] S. Gupta, M. Narajczyk, K. Bury, M. Sawczak, R. Bogdanowicz, Insights into Heterogeneous Electrochemical Performance of Boron-Doped Carbon Nanowall/Diamond Interfaces Using Mott-Schottky Analysis and Scanning Electrochemical Microscopy, 2026 submitted.
[42] A. Erdemir, G. Fenske, A. Krauss, D. Gruen, T. McCauley, R. Csencsits, Tribological properties of nanocrystalline diamond films, Surf. Coat. Technol. 120 (1999) 565–572, https://doi.org/10.1016/S0257-8972(99)00443-0.
[43] D. Das, A. Roy, Growth of nanostructured diamond films on glass substrates by low-temperature microwave plasma-enhanced chemical vapor deposition for applications in nanotribology, ACS Appl. Nano Mater. 5 (2022) 3558–3571.
[44] S. Gupta, B.R. Weiner, G. Morell, Investigations of the electron field emission properties and microstructure correlation in sulfur-incorporated nanocrystalline carbon thin films, J. Appl. Phys. 91 (2002) 10088.
[45] X. Guo, Y. You, A. Bao, P. Jia, J. Xiong, J. Li, Recent progress of nanodiamond film in controllable fabrication and field emission properties, Nanomaterials 13 (3) (2023) 577, https://doi.org/10.3390/nano13030577.
[46] A.V. Sumant, D.S. Grierson, J.E. Gerbi, J. Birrell, U.D. Lanke, O. Auciello, J. A. Carlisle, R.W. Carpick, Toward the ultimate tribological interface: surface chemistry and nanotribology of ultrananocrystalline diamond, Adv. Mater. 17 (2004) 1039.
[47] S. Gupta, O.A. Williams, R.J. Patel, K. Haenen, Residual stress, intermolecular force, and frictional properties distribution maps of diamond films for micro- and nano-electromechanical (M/NEMS) applications, J. Mater. Res. 21 (2006) 3037–3046.
[48] J.A. Baimova, An overview of mechanical properties of diamond-like phases under tension, Nanomaterials 14 (2) (2024) 129.
[49] J. Robertson, Diamond-like carbon, Philos. Mag. B 76 (1997) 335.
[50] F. Zhao, A. Vrajitoarea, Q. Jiang, X. Han, A. Chaudhary, J.O. Welch, R.B. Jackman, Graphene-nanodiamond heterostructures and their application to high current devices, Sci. Rep. 5 (2015) 13771, https://doi.org/10.1038/srep13771.
[51] R.E. Rawles, S.F. Komarov, R. Gat, W.G. Morris, J.B. Hudson, M.P. D'Evelyn, Mechanism of surface smoothing of diamond by a hydrogen plasma, Diam. Relat. Mater. 6 (1997) 791.
[52] M. Tsigkourakos, T. Hantschel, K. Arstila, W. Vandervorst, Diamond nanoparticle seeding for tip moulding application, Diam. Relat. Mater. 35 (2013) 14–18.
[53] J.L. Hutter, J. Bechhoefer, Calibration of atomic-force microscope tips, Rev. Sci. Instrum. 64 (1993) 1868–1873.
[54] A.D. Slattery, A.J. Blanch, J.S. Quinton, C.T. Gibson, Accurate measurement of Atomic Force Microscope cantilever deflection excluding tip-surface contact with application to force calibration, Ultramicroscopy 131 (2013) 46–55.
[55] G. Binnig, C.F. Quate, C. Gerber, Atomic Force Microscope, Phys. Rev. Lett. 56 (1986) 930–933.
[56] H. Olajumoke, O.H. Olubowale, S. Biswas, G. Azom, B.L. Prather, S.D. Owoso, K. C. Rinee, K. Marroquin, K.A. Gates, M.B. Chambers, A. Zu, J.C. Garno, "May be the force be with you!" Force-volume mapping with atomic force microscopy, ACS Omega 6 (2021) 25860–25875.
[57] J.H. Hoh, W.F. Heinz, A. A-Hassan, Support Note No. 240 Part B Digital Instruments, 1997.
[58] K.L. Johnson, K. Kendall, A.D. Roberts, Surface energy and the contact of elastic solids, Philos. Trans. R. Soc. A Math. Phys. Eng. Sci. 324 (1971) 301–313.
[59] B.V. Derjaguin, V.M. Muller, Y.P. Toporov, Effect of contact deformations on the adhesion of particles, J. Colloid Interface Sci. 53 (2) (1975) 314–326.
[60] B.D. Cullity, S.R. Stock, Elements of X-ray Diffraction, 3rd Ed, Pearson, 2014.
[61] M.A. Pimenta, G. Dresselhaus, M.S. Dresselhaus, L.G. Cancado, A. Jorio, R. Saito, Studying disorder in graphite-based systems by Raman spectroscopy, Phys. Chem. Chem. Phys. 9 (2007) 1276.
[62] S. Gupta, R.S. Katiyar, D.R. Gilbert, R.K. Singh, G. Morell, Microstructural studies of diamond thin films grown by electron cyclotron resonance-assisted chemical vapor deposition, J. Appl. Phys. 88 (2000) 5695.
[63] L. Bergmann, R.J. Nemanich, Raman and photoluminescence analysis of stress state and impurity distribution in diamond thin films, J. Appl. Phys. 78 (1995) 6709.
[64] N.G. Shang, P. Papakonstantinou, M. McMullan, M. Chu, A. Stamboulis, A. Potenza, S.S. Dhesi, H. Marchetto, Catalyst-free efficient growth, orientation and biosensing properties of multilayer graphene nanoflake films with sharp edge planes, Adv. Funct. Mater. 18 (2008) 3506–3514.
[65] Y. Yu, P. Qiao, T. Chong, Z. Shen, Carbon nanowalls grown by microwave plasma enhanced chemical vapor deposition, Adv. Mater. 14 (1) (2002) 64–67.
[66] C. Gu, W. Li, J. Xu, S. Xu, C. Lu, L. Xu, J. Li, S. Zhang, Graphene grown out of diamond, Appl. Phys. Lett. 109 (2016) 162105.
[67] K. Kobayashi, M. Tanimura, H. Nakai, A. Yoshimura, H. Yoshimura, K. Kojima, M. Tachibana, Nanographite domains in carbon nanowalls, J. Appl. Phys. 101 (2007) 094306-1–094306-4.
[68] M. Hiramatsu, Y. Nihashi, H. Kondo, M. Hori, Nucleation control of carbon nanowalls using inductively coupled plasma-enhanced chemical vapor deposition, Jpn. J. Appl. Phys. 52 (2013) 01AK05.
[69] Z.V. Živcová, V. Petrak, O. Frank, L. Kavan, Electrochemical impedance spectroscopy of polycrystalline boron doped diamond layers with hydrogen and oxygen terminated surface, Diam. Relat. Mater. 55 (2016) 70–76.
[70] J.-H. Lee, E.K. Lee, W.-J. Joo, Y. Jang, B.-S. Kim, J.Y. Lim, S.-H. Choi, S.J. Ahn, J. R. Ahn, D. Whanget, Wafer-scale growth of single-crystal monolayer graphene on reusable hydrogen-terminated germanium, Science 344 (2014) 286–289.
[71] A.V. Sumant, O. Auciello, R.W. Carpick, S. Srinivasan, J.E. Butler, Ultrananocrystalline and nanocrystalline diamond thin films for MEMS/NEMS applications, MRS Bull. 35 (2010) 281–288.
[72] Z. Pan, H. Sun, Y. Zhang, C. Chen, Harder than diamond: superior indentation strength of wurtzite BN and lonsdaleite, Phys. Rev. Lett. 102 (2009) 055503.
[73] C. Lee, X. Wei, J.W. Kysar, J. Hone, Measurement of the elastic properties and intrinsic strength of monolayer graphene, Science 321 (2008) 385–388.
[74] S. Chen, X. Xu, X. Liu, Y. Zheng, J.A. Duan, Improved wear resistant and its atomistic mechanism of graphene-modified diamond heterostructure in micro-machining, Appl. Surf. Sci. 722 (2026) 165580.
[75] S. Chen, W. Bai, S. Wang, H. Wang, W. Guo, Y. Dou, Surface-dependent adhesion properties of graphene on diamonds for the fabrication of nanodevices: a molecular dynamics investigation, ACS Appl. Nano Mater. 6 (4) (2023), 2942–295.
[76] M. Radmacher, J.P. Cleveland, M. Fritz, H.G. Hansma, P.K. Hansma, Mapping interaction forces with the atomic force microscope, Biophys. J. 66 (6) (1994) 2159–21651.
[77] H.J. Butt, B. Capella, M. Kappl, Force measurements with the atomic force microscope: technique, interpretation, and applications, Surf. Sci. Rep. 59 (1–6) (2005) 1–152.
[78] J.J. Bang, S.R. Russell, K.K. Rupp, S.A. Claridge, Multimodal scanning probe imaging: nanoscale chemical analysis from biology to renewable energy, Anal. Methods 7 (2015) 7106–7127.
[79] M.E. McConney, S. Singamaneni, V.V. Tsukruk, Probing soft matter with the atomic force microscopies: imaging and force spectroscopy, Polym. Rev. 50 (2010) 235–286.
[80] J. Domke, S. S. Dannohl, W.J. Parak, O. Muller, W.K. Aicher, M. Radmacher, Substrate dependent differences in morphology and elasticity of living osteoblasts investigated by atomic force microscopy, Colloids Surf. B: Biointerfaces 19 (2000) 367–379.
[81] J.P. Cleveland, S. Manne, D. Bocek, P.K. Hansma, A nondestructive method for determining the spring constant of cantilevers for scanning force microscopy, Rev. Sci. Instrum. 64 (1993) 403–405.
[82] M. Grimsditch, E. Anastassakis, M. Cardona, Brillouin scattering study of diamond elastic constants, Phys. Rev. B 18 (1978) 901.
[83] R. Ramírez, C.P. Herrero, Elastic properties and mechanical tension of graphene, hys. Rev. B 95 (2017) 045423.
[84] A.S. Machado, D. Maroudas, A.R. Muniz, Tunable mechanical properties of diamond superlattices generated by interlayer bonding in twisted bilayer graphene, Appl. Phys. Lett. 103 (2013) 013113.
[85] Y. Wu, Y.-M. Lin, A.A. Bol, K.A. Jenkins, F. Xia, D.B. Farmer, Y. Zhu, Ph. Avouris, High-frequency, scaled graphene transistors on diamond-like carbon, Nature 472 (2011) (2011) 74–78.
[86] J. Wang, L. Li, J. Wang, W. Yang, P. Guo, M. Li, D. Liu, H. Zeng, B. Zhao, First-principles study on the nanofriction properties of diamane: the thinnest diamond film, Nanomaterials 12 (17) (2022) 2939:1–2939:12.
[87] C.A. Klein, G.F. Cardinale, Young's modulus and Poisson's ratio of CVD diamond, Diam. Relat. Mater. 2 (1993) 918–923.
[88] D. Selli, I. Baurin, S. Leoni, Z. Zhu, D. Tománek, G. Seifert, Theoretical investigation of the electronic structure and quantum transport in the graphene-C (111) diamond surface system, J. Phys. Condens. Matter 25 (2013) 435302.
[89] K.C. Pandey, New dimerized-chain model for the reconstruction of the diamond (111)-(2×1) surface, Phys. Rev. B 25 (1982), 4338(R).
[90] K. Kendall, The adhesion and surface energy of elastic solids, Phys. D: Appl. Phys. 4 (8) (1971) 1186–1195.
[91] S. Das, D. Lahiri, D.Y. Lee, A. Agarwal, W. Choi, Measurements of the adhesion energy of graphene to metallic substrates, Carbon 59 (2013) 121–129.
[92] X. He, Q. Bai, R. Shen, F. Zhang, Y. Guo, The evolution of configuration and final state of graphene on rough iron surface, Appl. Surf. Sci. 530 (2020) 147084.
[93] S. Kanada, M. Nagai, S. Ito, T. Matsumoto, M. Ogura, D. Takeuchi, S. Yamasaki, T. Inokuma, N. Tokuda, Fabrication of graphene on atomically flat diamond (111) surfaces using nickel as a catalyst, Diam. Relat. Mater. 75 (2017) 105–109.
[94] T. Tanaka, M. Kozako, N. Fuse, Y. Ohki, Proposal of a multi-core model for polymer nanocomposite dielectrics, IEEE Trans. Dielectr. Electr. Insul. 12 (4) (2005) 669–681.